

6-26-2015

Computational Analysis of Flow Around a Scaled Axial-Flow Hydro Turbine

Andrew W. Murphy

Follow this and additional works at: https://digitalrepository.unm.edu/me_etds

Recommended Citation

Murphy, Andrew W.. "Computational Analysis of Flow Around a Scaled Axial-Flow Hydro Turbine." (2015).
https://digitalrepository.unm.edu/me_etds/32

This Thesis is brought to you for free and open access by the Engineering ETDs at UNM Digital Repository. It has been accepted for inclusion in Mechanical Engineering ETDs by an authorized administrator of UNM Digital Repository. For more information, please contact disc@unm.edu.

Andrew W. Murphy

Candidate

Mechanical Engineering

Department

This thesis is approved, and it is acceptable in quality and form for publication:

Approved by the Thesis Committee:

Dr. Svetlana V. Poroseva, Chairperson

Dr. Charles R. Truman

Dr. Peter Vorobieff

**COMPUTATIONAL ANALYSIS OF FLOW AROUND
A SCALED AXIAL-FLOW HYDRO TURBINE**

By

ANDREW W. MURPHY

B.S., MECHANICAL ENGINEERING, UNM 2012

THESIS

Submitted in Partial Fulfillment of the
Requirements for the Degree of

Master of Science

M.S., Mechanical Engineering

The University of New Mexico
Albuquerque, New Mexico

May, 2015

©2015 Andrew W. Murphy

DEDICATION

I would like to dedicate thesis with love and adoration to the most supportive and caring woman I know, Miranda Qualls. Without her support and dedication to our family this research would not be possible. Thank you for everything you have done and continue to do for me and our family.

*“The three great essentials to achieve anything worthwhile are: hard work,
stick-to-itiveness, and common sense.”*

-Thomas A. Edison

ACKNOWLEDGMENTS

I would first like to thank my father and mother, Kevin and Susan Murphy. Their humble advice, compassion, and support have allowed me to do many things including this thesis. They have always been a source of encouragement and inspiration throughout my life. I would like to thank my advisor Svetlana Poroseva for her support and direction in completing this work. Throughout this research Vincent Neary has been an excellent mentor and teacher his advice and guidance inspired this research. Lastly, I would like to acknowledge Sandia National Laboratories and the Department of Energy for their computational resources and access to experimental data that made this research possible.

COMPUTATIONAL ANALYSIS OF FLOW AROUND A SCALED AXIAL-FLOW HYDRO TURBINE

By

ANDREW W. MURPHY

B.S., MECHANICAL ENGINEERING, UNM, 2012

M.S., MECHANICAL ENGINEERING, UNM, 2015

ABSTRACT

Water power energy harvesting has become an important and growing industry supported by research and significant interest and impetus from the government and commercial sector. Due to water's high power density, marine current energy is an attractive addition to other renewable energy technologies. That said, there is still much to be understood about the design, application, installation, operation, and maintenance of current-driven marine-hydrokinetic devices and with new designs coming out frequently it is imperative to understand the physics and dynamics involved.

Recently, testing of the Sandia turbine, designed by University of California, Davis, Pennsylvania State and Sandia National Laboratories, took place at Pennsylvania State's Applied Research Laboratory. The testing was performed with a 1:8.7 scale model of the Sandia turbine. The experiment successfully assessed the turbine's power and cavitation performance, unsteady driveshaft loading, blade strain, unsteady tower pressure, flow field, and acoustics. Given the expense and time required for experimentation, commercial computational fluid dynamics codes, such as CD-Adapco's Star-CCM+ can be used to simulate new designs both quickly and inexpensively. The goal of this research is to validate the results obtained using Star CCM+ to model the Sandia turbine as compared to the experimental results obtained by Pennsylvania State.

To carry out the simulation, several unstructured grids were generated on which several unsteady simulations were run at the design point of a tip-speed ratio of 4. For this design point at 95% blade span, the chord Reynolds number is approximately 500,000 which equates to about 2,000,000 for the full scale turbine. In comparing model results to experimental data there was good agreement for power performance parameters, such as thrust and power coefficients, as well as downstream velocity profiles. With such good agreement it is optimistic that computational fluid dynamics models can be used to accurately predict the performance of future water turbine designs, thus reducing the high cost of research needed to develop novel current-driven marine-hydrokinetic devices.

TABLE OF CONTENTS

LIST OF FIGURES	vii
LIST OF TABLES	ix
I. INTRODUCTION	1
II. TURBINE DESIGN.....	6
III. COMPUTATIONAL APPROACH.....	7
A. Experimental Setup.....	7
B. Computational Domain.....	8
C. Grid	9
D. Boundary Conditions	12
E. Turbulence Model Selection	13
F. Numerical Methods.....	17
IV. Results.....	19
A. Grid Sensitivity	19
B. Simulation.....	27
1. Power Performance	28
2. Velocity Profiles.....	34
3. Reynolds Stress	38
4. Unsteady Tower Pressure.....	43
5. Experimental Uncertainty	45
V. Conclusion	55
VI. References.....	58

LIST OF FIGURES

FIGURE 1: LOW-FIDELITY CFD COMPARISON WITH EXPERIMENTAL DATA OF POWERING PERFORMANCE I.E. THRUST COEFFICIENT (C_T), POWER COEFFICIENT (C_p) AND TORQUE COEFFICIENT (C_Q) OF THE SANDIA TURBINE. WHERE DASHED BLACK LINE IS DESIGN THRUST COEFFICIENT, SOLID BLACK LINE IS DESIGN POWER COEFFICIENT AND DOTTED BLACK LINE IS DESIGN TORQUE COEFFICIENT. [8].....	4
FIGURE 2: SANDIA TURBINE CAD GEOMETRY AND MANUFACTURED TURBINE [8].....	6
FIGURE 3: CAD ASSEMBLY OF THE ARL EXPERIMENTAL SETUP [8]	7
FIGURE 4: COORDINATE SYSTEM DEFINITION.....	8
FIGURE 5: CASE 1 UNSTRUCTURED MESH USED IN SANDIA TURBINE SIMULATION	11
FIGURE 6: CASE 1 3D VIEW OF CELLS FOR THE GRID USED IN SANDIA TURBINE SIMULATION	11
FIGURE 7: INSTANTANEOUS VELOCITY CONTOUR PLOTS OF A) CASE 1, B) CASE 2, C) CASE 3, AND D) CASE 4 MESHES	20
FIGURE 8: V_x VELOCITY PROFILES AT SPECIFIED AXIAL LOCATIONS ($x = -800$ MM TO 135 MM, $z = 0$ MM)	21
FIGURE 9: V_x VELOCITY PROFILES AT SPECIFIED AXIAL LOCATIONS ($x = 216$ MM TO 574 MM, $z = 0$ MM) AND $x = 574$ MM, $z = \pm 19$ MM LEFT AND RIGHT OF TURBINE CENTERLINE	21
FIGURE 10: REVOLUTION AVERAGED POWER, TORQUE, AND THRUST COEFFICIENTS OBTAINED THROUGH THE SIMULATIONS AS A FUNCTION OF THE NUMBER OF CELLS IN THE GRID COMPARED WITH EXPERIMENTAL DATA.....	22
FIGURE 11: SINGLE REVOLUTION TORQUE COEFFICIENT HISTORY OF SIMULATION AND TIME-AVERAGED EXPERIMENTAL DATA	30
FIGURE 12: SINGLE REVOLUTION THRUST COEFFICIENT HISTORY OF SIMULATION AND EXPERIMENTAL DATA	32
FIGURE 13: SINGLE REVOLUTION POWER COEFFICIENT HISTORY OF SIMULATION AND EXPERIMENTAL DATA	33
FIGURE 14: ARL EXPERIMENTAL SETUP AND MEASUREMENT LOCATIONS FOR FLOW FIELD QUANTIFICATION [8]	34
FIGURE 15: V_x VELOCITY PROFILES AT SPECIFIED AXIAL AND TANGENTIAL LOCATION ($z = 0$ MM UNLESS SPECIFIED OTHERWISE) FOR SIMULATION AND EXPERIMENTAL DATA	36
FIGURE 16: V_z VELOCITY PROFILES AT SPECIFIED AXIAL AND RADIAL LOCATION ($z = 0$ MM UNLESS SPECIFIED OTHERWISE) FOR SIMULATION AND EXPERIMENTAL DATA.....	38

FIGURE 17: AXIAL REYNOLDS STRESS PROFILES AT SPECIFIED LOCATIONS FOR SIMULATION AND EXPERIMENTAL DATA	39
FIGURE 18: AXIAL REYNOLDS STRESS DETAIL PICTURE FOR $x = 64$ MM, 135 MM, 216 MM, AND 574 MM DOWNSTREAM OF TURBINE.....	40
FIGURE 19: RADIAL REYNOLDS STRESS AT SPECIFIED AXIAL LOCATIONS FOR SIMULATION AND EXPERIMENT	41
FIGURE 20: RADIAL REYNOLDS STRESS DETAIL PICTURE FOR $x = 64$ MM, 135 MM, 216 MM, AND 574 MM	42
FIGURE 21: TOWER PRESSURE COEFFICIENT AT SPECIFIED RADIAL POSITIONS ALONG TOWER FOR SIMULATION AND EXPERIMENTAL DATA. DISTANCE IS SPECIFIED AS PERCENTAGE OF TURBINE BLADE SPAN.	44
FIGURE 22: SINGLE REVOLUTION TORQUE COEFFICIENT HISTORY FOR SIMULATION AND EXPERIMENT WITH ERROR IN GREY	48
FIGURE 23: SINGLE REVOLUTION THRUST COEFFICIENT HISTORY FOR SIMULATION AND EXPERIMENT WITH ERROR IN GREY	49
FIGURE 24: SINGLE REVOLUTION POWER COEFFICIENT HISTORY FOR SIMULATION AND EXPERIMENT WITH ERROR IN GREY	50
FIGURE 25: V_x AND V_z VELOCITY PROFILES WITH ERROR IN GREY ON EXPERIMENTAL DATA FOR $x = -800$ MM AND -17 MM	51
FIGURE 26: V_x AND V_z VELOCITY PROFILES WITH ERROR IN GREY ON EXPERIMENTAL DATA FOR $x = 64$ MM AND 89 MM	51
FIGURE 27: V_x AND V_z VELOCITY PROFILES WITH ERROR IN GREY ON EXPERIMENTAL DATA FOR $x = 135$ MM AND 216 MM	52
FIGURE 28: V_x AND V_z VELOCITY PROFILES WITH ERROR IN GREY ON EXPERIMENTAL DATA FOR $x = 250$ MM AND 574 MM	53
FIGURE 29: V_x AND V_z VELOCITY PROFILES WITH ERROR IN GREY ON EXPERIMENTAL DATA FOR $x = 574$ MM AND $z = 19$ MM AND -19 MM.....	53

LIST OF TABLES

TABLE 1: MESH NAMING CONVENTIONS AND BASIC INFORMATION.....	10
TABLE 2: GENERAL MESH STATISTICS-ROTATING REGION	12
TABLE 3: GENERAL MESH STATISTICS-STATIONARY REGION	12
TABLE 4: GRID CONVERGENCE AND APPARENT ORDER FOR CASES 1-4.....	24
TABLE 5: REVOLUTION AVERAGED POWER PERFORMANCE COEFFICIENTS AND RELATIVE DIFFERENCE COMPARED TO EXPERIMENTAL VALUES	31
TABLE 6: SURVEY LOCATIONS FOR FLOW FIELD LDV MEASUREMENTS	35

I. INTRODUCTION

Research and development of current-driven marine-hydrokinetic (MHK) devices is important because it is an untapped area of renewable energy. Unlike wind turbines, which have been around for decades and have, for the most part, been accurately characterized and for which an optimized design has been found, current-driven MHK devices and technology is still in its infancy but shows promise as a viable and reliable source of renewable energy. As context for this potential it is noted that the estimated available ocean current energy in North America is 163 TWh [1]. Combined, the rivers in the United States were evaluated and determined to have approximately 120 TWh of extractable current energy [1]. The energy potential that these sites represent is staggering yet it still remains to be seen if MHK technologies can be developed to effectively capture it. Approximately 85,000 homes can be powered by 1 TWh [1].

Clearly in the early stages of development, current-driven MHK devices require a great deal of research and development. According to the Electric Power Research Institute, there are several key areas in which improvement is needed. These areas include: (1) numerical tools and software for system design and optimization, (2) materials, composites, corrosion and anti-fouling, (3) modeling that captures the fundamental physics in order to improve the accuracy and detail of existing knowledge, (4) models that enable a better understanding of hydrodynamic and primary power conversion, and (5) experimental and deployment results to be used to establish guidelines and standards [2]. This last research area is needed because continued deployment and testing will enable initial guidelines to be verified, allowing for the establishment of industry and government standards.

Several companies have already designed, tested and deployed prototypes and/or full scale current-driven MHK devices. Again, with research being in the early stages there are only a few companies with current-driven MHK turbines. Several companies with MHK devices include: SeaGen, OpenHydro and Voith. SeaGen developed the SeaGen S which is an axial-flow, tidal turbine. In its current design it boasts the largest swept area of any available ocean current-driven turbines. Also this turbine was designed to operate in bi-directional flows with a 48% efficiency over a broad range of current velocities [3]. OpenHydro's turbine is an open center turbine, which is similar in design to a rim-driven wind turbine [4]. Voith has designed and deployed a horizontal axial-flow turbine with a symmetric blade profile for bi-directional operation [5].

Many researchers have conducted scale-model testing or CFD simulations of current-driven MHK devices. However, very little literature is available that directly compares CFD simulations of the exact experimental setup to experimental data. This is largely due to the expense of experimentation and CFD simulations. It is often too financially burdensome to conduct both an experiment and computational fluid dynamics simulations. However, an example of recent research was an experiment of an axial-flow hydrokinetic turbine with a scale-model turbine rotor diameter of 0.8 m [6]. The experiment performed by Bahaj *et al.* took place in the Towing Tank at South Hampton Institute. Through experimentation both power and thrust coefficient data for the turbine was obtained. It was also determined that turbine tip immersion depth was an important factor on the turbine's ability to extract the energy from flowing water. This research determined that it was necessary to design an MHK turbine for a specific depth of water in which to operate. In this case, the turbine was operated under various conditions,

including, tip-speed ratios (TSR's) from 2 to 7 and a variety of hub pitch angles. It was concluded that the optimal operating conditions for this specific turbine were TSR's from 5 to 7 and a hub pitch angle of approximately 20°. Lastly, it was observed that the turbine suffered significant reductions in power when it was operated in a yawed position.

In other research, Kang *et al.* performed numerical simulations of 3D flow past a marine-hydrokinetic turbine [7]. The novelty of this research was the use of a high resolution grid with the large eddy simulation (LES) turbulence model. The maximum number of nodes used was 185 million. With these simulations it was determined that the downstream wake of a MHK turbine consists of three distinct regions, the first region is an outer layer with tip vortices rotating in the same direction as the blades, the second region consists of a counter-rotating inner layer and the third layer is comprised of a core-layer which co-rotates with respect to the tip vortices. Through these simulations it was concluded that CFD was a promising tool for designing real-life MHK devices of similar geometry.

Previous research has been performed on the Sandia turbine [8], however, it has been limited in scope. The Sandia turbine was the result of a joint research effort by University of California at Davis (UC-Davis), Sandia National Laboratories (SNL), and Pennsylvania State (Penn State). Scale model testing of the Sandia turbine took place at Penn State's Applied Research Laboratory (ARL). To validate low-fidelity approximations to loading and performance brief finite element analysis (FEA) and unsteady Reynolds averaged Navier Stokes (RANS) CFD simulations were conducted [9]. The CFD simulations were carried out under the largest expected loading condition.

The force loading results from these simulations were used to verify the spanwise loading calculated with an in-house blade element method (BEM) code from Pennsylvania State's ARL [9]. Favorable comparisons were found between the tunnel test data and results from ARL's BEM code for power performance. The blade-loadings and powering data are in line with expectations from the BEM model except for the results at 7 m/s which is due to cavitation breakdown, (Figure 1).

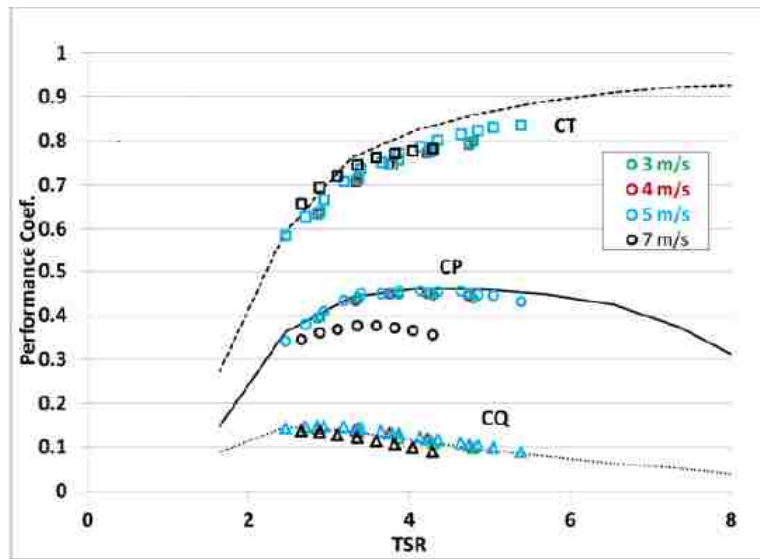


Figure 1: Low-fidelity CFD comparison with experimental data of powering performance i.e. thrust coefficient (C_T), power coefficient (C_P) and torque coefficient (C_Q) of the Sandia turbine. Where dashed black line is design thrust coefficient, solid black line is design power coefficient and dotted black line is design torque coefficient. [8]

In addition to the work previously cited, results from an unsteady CFD simulation of a current-driven turbine were compared by [10] to the experimental results of [6]. Unsteady simulations were used to capture time-accurate flow characteristics due to the flow past the MHK turbine [10]. At the time of publication only coarse mesh results were available and, as expected, there was reasonable agreement between simulation and experimental results which could improve with grid refinement. The main conclusion, as

with most CFD simulations, was that the main challenge in obtaining good agreement with experimental results was developing a good mesh.

The research conducted and presented herein compares the simulated results of a scaled-model of the Sandia turbine [11] to experimental results obtained by the Pennsylvania State University's Applied Research Laboratory (ARL) [8]. Previous work by [6], [7], [9], and [10] have either performed experiments of axial-flow MHK turbines or carried out CFD simulations of axial-flow MHK turbines. Research has yet to be published comparing CFD simulation results that are a direct replica of an experiment with experimental results. To validate the simulation results, a simulation under design and experimental conditions was run to determine the level of accuracy of the unsteady Reynolds-averaged Navier-Stokes (URANS) computational fluid dynamics (CFD) models by comparison with results from experiments. Comparisons are made for a variety of parameters including, power performance i.e., power, torque, and thrust coefficients, velocity profiles, Reynolds stress, and tower pressure. Additionally, an uncertainty analysis of the experimental data was performed for the power performance coefficients and velocity profiles.

II. TURBINE DESIGN

This research covers the computational analysis of a new design of an axial-flow hydro-turbine and hydrofoil family [11]. The hydro-turbine blade is composed of three different hydrofoils designed with consideration of current leading wind turbine blade geometries. The inboard 40% of the blade is composed of the MHKF1-400 hydrofoil that has a fatback trailing edge to aid in blade strength as well as supporting flow attachment on large thickness-ratio foils. From 40% to 75% of blade span the MHKF1-240s hydrofoil was used in an effort to provide structural support of the rotor blades as well as a substantial amount of power production. The trailing edge of this hydrofoil and the outboard hydrofoil were designed to reduce blade singing which is a hydroacoustic, hydroelastic phenomenon where vortex shedding can induce audible harmonic tones or trailing edge vibrations [8]. Lastly, for the outboard hydrofoil, 75% to 100% of the blade span, the MHKF1-180s foil was used. This foil is similar in profile to the mid-board profile; however, the thickness was reduced by 25% from 0.240c to 0.180c. Detailed information on the design and predicted performance of the MHKF1 hydrofoil family can be found in [11]. Both the CAD model and manufactured scale-model turbine are shown in Figure 2.



Figure 2: Sandia turbine CAD geometry and manufactured turbine [8]

III. COMPUTATIONAL APPROACH

A. Experimental Setup

The following results and discussion pertain to a simulation of the Sandia turbine and the corresponding experimental data obtained from ARL. ARL performed several experiments to characterize the flow field both upstream and downstream of the turbine. Experimental data for the flow field is available for the design condition of 5 m/s inflow and 664 RPM. Temporal and spatial data of velocity profiles were collected using laser Doppler velocimetry (LDV) while planar /spatial velocity data was collected using particle image velocimetry [8]. Additionally, ARL performed a battery of power performance tests at discrete inflow velocities, ranging from 2 m/s to 7 m/s in 1 m/s increments, and varied the RPM to obtain powering coefficients for a range of TSR's, approximately 2.5-5.75. At the design point, at 95% blade span, the chord Reynolds number is approximately 500,000 which equates to about 2,000,000 for the full scale turbine. Blockage effects were present in the experiment however the tunnel walls were modeled thus no correction is necessary. The following comparisons are made for a simulation performed under the design conditions.



Figure 3: CAD assembly of the ARL experimental setup [8]

B. Computational Domain

The computational domain was modeled to exactly match the experimental setup described in [13]. The 1:8.7 scale-model Sandia turbine was tested in ARL's Garfield Thomas water tunnel, which is a 1.22m diameter by 4.27m long recirculating water tunnel [8]. The computational domain consists of a 1.22m diameter by 9.33m long tunnel with the turbine positioned 3.6m downstream of the inlet and 5.73m upstream of the outlet. The turbine consists of three blades composed of the aforementioned hydrofoils and has a diameter of 574mm. The tower and nacelle diameters were 76.2mm with a base-of-tower to rotor-center height of 0.61m. The coordinate system is shown in Figure 4, where the positive x-axis is defined as downstream of the rotor nacelle, the positive y-axis points from the rotor nacelle toward the tower side of the tunnel and the positive z-axis is perpendicular to the y-axis pointing towards the top of the tunnel.

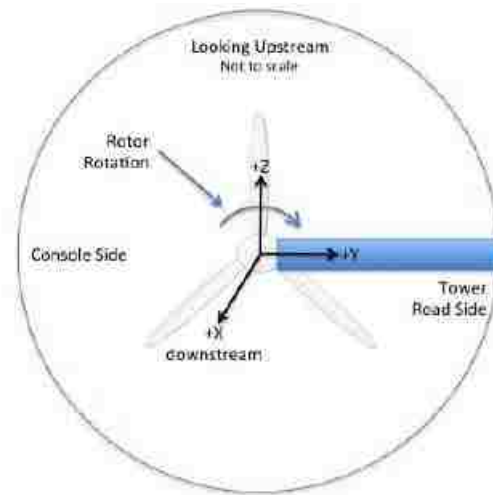


Figure 4: Coordinate system definition

C. Grid

For the comparison of experimental results with those obtained using commercial CFD code, several grids were generated. These grids were composed of unstructured polyhedral cells. Although there is research to suggest that solutions obtained on unstructured grids inherently have more error than structured grids due to their semi-random construction [12]. The unstructured grid approach was chosen due to the complex geometry of the hydro-turbine blades and for ease of grid generation. As with structured meshes the polyhedral cells of the unstructured mesh remain orthogonal to the flow direction thus providing an approximate solution, given sufficient grid discretization. A method for defining grid spacing in Star CCM+ is to define a base size, i.e. 0.5 m, which is used to describe other meshing parameters as described below.

All meshes are composed of a rotating region which encompasses the nacelle and rotor and a stationary region which includes the tower and tunnel walls. Three grids were created based on the same percentages of a mesh cell base size. Each grid is assigned a Case number with Case 1 being the coarsest grid and Case 4 being the finest grid. Cases 1 and 2 used a base size of 0.09 m and 0.068 m respectively, while Cases 3 and 4 had a base size of 0.05 m. Cases 1-3 were meshed with 12 prism layers with an absolute height of 2.5mm, a prism layer stretching factor of 1.5, and the first cell is located at a distance of 2.89×10^{-5} m from the wall. This prism layer thickness corresponds to 1% of the turbine rotor radius or 0.01R. The rotor was meshed using minimum and target sizes of 0.1% and 1% of the base size respectively. The wake was refined five diameters downstream of the turbine with symmetric polyhedral cells that corresponded to 10% of the base size. Additionally, the tower was meshed using minimum and target sizes of 1%

and 8% of the base respectively. The cell density and growth were controlled by a factor of 1.0 for the rotor, tower, and refined wake. The remainder of the domain was meshed using a surface growth rate of 1.2 with a minimum surface size of 15% and target surface size of 25% of the base.

The Case 4 mesh was created using the same meshing parameters as Case 3 except for the number of prism layers and size of the prism layer. For Case 4 the number of prism layers was 20 with an absolute thickness of 6.6 mm which corresponds to approximately 2.5% of the radius (0.025R). The distance between the wall and the first cell was 2.98×10^{-6} m. This last grid was generated to determine what effect the number and size of prism layers has on the accuracy of the solution. Figures 5 and 6 show the Case 1 mesh projected on the x-y plane along the centerline of the turbine and the 3D view of the generated mesh respectively. Figure 5 illustrates the meshing scheme where the wake, rotor and tower are more refined than outer areas. Figure 6 shows how the cell volume changes throughout the computational domain. The flow direction in Figure 5 and 6 is from left to right. The naming convention and basic mesh statistics for all meshes are shown in Table 1.

Table 1: Mesh naming conventions and basic information

Simulation/Grid Name	Number of Cells	Mesh Base Size (m)	Number of Prism Layers	Height of Prism Layer (mm)
Case 1	7,958,112	0.09	12	2.5
Case 2	12,551,180	0.068	12	2.5
Case 3	28,167,672	0.05	12	2.5
Case 4	31,850,855	0.05	20	6.6

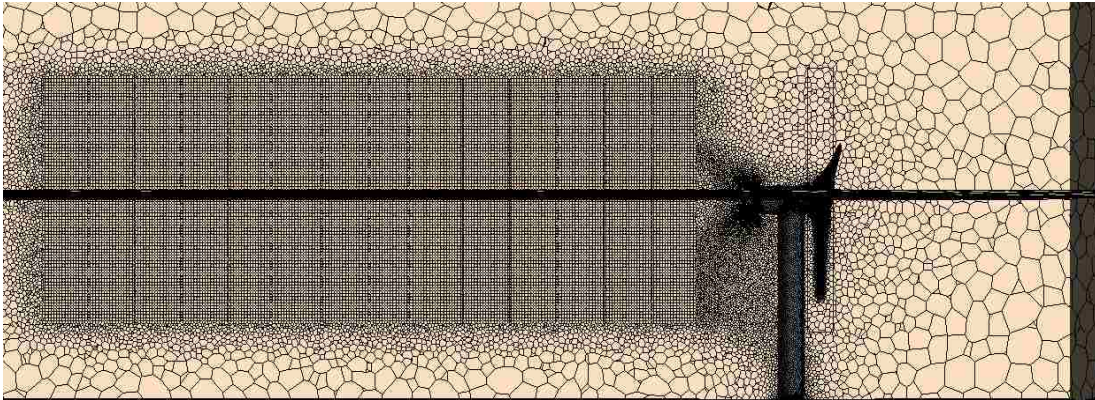


Figure 5: Case 1 unstructured mesh used in Sandia turbine simulation

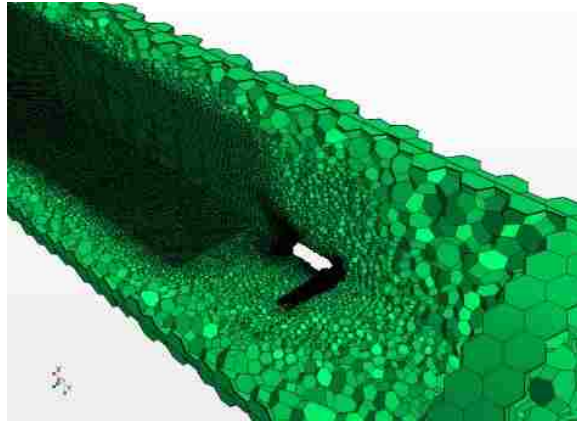


Figure 6: Case 1 3D view of cells for the grid used in Sandia turbine simulation

Tables 2 and 3 list the mesh statistics of importance including maximum skewness angle and cell volume change for the rotating and stationary regions. There were no negative volume cells present in any of the meshes. Ideally, the maximum skewness angle for an unstructured mesh is between 80° and 90° ; however, in practice, this is rarely the case [13]. The highest skewness angle of 118.43° was present in the stationary region of the Case 1 mesh. All other skewness angles were within 30° of the ideal value and these values are within the accepted range [14]. Through further investigation it was found that this maximum skewness angle is isolated to one cell,

however, a study was not performed to determine the average skewness angle of each case which may give further insight into the quality of the generated meshes.

Table 2: General Mesh Statistics-Rotating Region

Name	Number of Cells	Max. Skewness Angle	No. Cells w/ Face Validity < 0.8	No. Cells w/ Volume Change < 1×10^{-3}
Case 1	4,341,799	101.43°	0	98
Case 2	4,819,564	85.6°	0	58
Case 3	9,181,806	114.5°	0	190
Case 4	12,890,395	114.5°	0	190

Table 3: General Mesh Statistics-Stationary Region

Name	Number of Cells	Max. Skewness Angle	Face Validity < 0.8	Volume Change < 1×10^{-3}
Case 1	3,616,313	118.43°	0	0
Case 2	7,731,616	85.6°	0	0
Case 3	18,985,866	87.37°	0	2
Case 4	18,960,460	113.94°	0	40

D. Boundary Conditions

The computational domain boundaries for the CFD simulations were as follows: inlet modeled as velocity inlet, rotor, tower and tunnel walls modeled as no-slip walls, and the outlet was modeled as a pressure outlet. The velocity inlet was modeled as a constant inlet profile with sufficient length to establish a turbulent velocity profile indicative of what was seen in the experiment. The tunnel used in the experiment was a closed-loop

setup thus no outlet existed. An approximation to this condition was to model the outlet of the simulation as a pressure outlet. For these simulations several initial conditions were applied. Specifically, the pressure at the outlet was set to have a zero pressure which corresponds to a gauge pressure of zero and an atmospheric, absolute, pressure of 101,325 Pa. A turbulence intensity of 0.01 was prescribed as an approximate to the turbulence intensity that was experienced in the water tunnel during testing [8]. The turbulent viscosity ratio was set to 10 and an inlet velocity of 5 m/s.

To accurately simulate the conditions under which the experiment took place several key parameters were specified. The turbine had an imposed rotation of 664 RPM, resulting in a tip-speed-ratio (TSR) of 4 which is an exact imitation of the conditions of the flow field characterization experiment. One difference between the experiment and simulation setup is that in the experiment the entrance had a reducing concentric cone shape. For the simulation no conical shaped entrance was employed. Additionally, for the experiment a dynamometer, used to measure power and torque, was attached to the turbine and no such geometry was added to the simulation. Although there are several differences between the experimental and simulation geometry no such discrepancies exist for the boundary conditions of the flow, i.e., turbulence intensity, density, velocity, rotation rate, etc.

E. Turbulence Model Selection

To ascertain what turbulence model to use for a rotating turbine in water it is important to first look at the available turbulence models and decide on a qualitative approach in selecting the model to use. In a given CFD software package there are

various turbulence models available for simulating the described flow with different degrees of accuracy and computational burden. These models include zero-, one-, and two-equation models which fall under the classification of Reynolds-Averaged Navier Stokes (RANS) models. Zero-equation or algebraic turbulence models do not model the transport of turbulence scales and thus have a very limited applicability. One-equation models compute the turbulent length however there is no transport of this length scale and no calculation of the velocity scale. Two-equation models compute both the length and velocity turbulence scales and have been shown to provide good results for many flows, with varying success [15]. There are a variety of zero-, one-, and two-equation models available in Star-CCM+ however a two-equation RANS model is best suited for this problem.

Three of the most popular two-equation turbulence models [16] are the standard $k-\varepsilon$ [17], realizable $k-\varepsilon$ [18], and the 2006 $k-\omega$ [19]. The standard $k-\varepsilon$ was the most widely used turbulence model prior to ~2005 [16]. It has been shown to have good results for isotropic (high Re) flows, simple flows, plane and radial jets (but not round jets), and plumes. Shortcomings of the standard $k-\varepsilon$ model include its inability to accurately predict the flow of round jets, far wakes, strongly curved surfaces, high swirl, flow separation, sudden acceleration, and low Re. The realizable $k-\varepsilon$ model is like the standard $k-\varepsilon$ model but it contains a realizability constraint that will only yield positive normal stresses. With this modification the realizable $k-\varepsilon$ model has improved results over the standard $k-\varepsilon$ for separated and swirling flows, as well as boundary flows, strong streamline curvature, and round jets [16]. However, the realizable $k-\varepsilon$ is not as stable as the standard $k-\varepsilon$. The newest model which has seen increased popularity is the 2006 $k-\omega$ model. This model

has been shown to be well suited for flows with adverse pressure gradients, separated flows, swirl and low-Reynolds number. The model does require a fine mesh near the wall and it is recommended that the first node be at $y^+ < 5$ [20].

The model that best meets all modeling requirements is the 2006 $k-\omega$ turbulence model. It is expected that there will be varying degrees of swirl, separated flow and that the Reynolds number is low. The 2006 $k-\omega$ turbulence model by Wilcox has been shown to dramatically improve predictive accuracy over the 1988 version [21] for free shear flows and strongly separated flows [19]. The 2006 $k-\omega$ is an eddy viscosity model which means the turbulent eddy viscosity is used in approximating the Reynolds stress term. In selecting a model it was preferred that the model selected be widely available in a variety of commercial software packages and well known for its ability to solve most turbulence problems so that future researchers may find benefit in using CFD to supplement or replace costly physical experiments.

The following analysis is provided to explain the equations and terms of the 2006 $k-\omega$ model. For any RANS model an approximation to the Reynolds stress tensor must be made. For the 2006 $k-\omega$ model the Boussinesq approximation is assumed valid and the Reynolds stress is defined as

$$\tau_{ij} = 2 \frac{\nu_T}{\rho} S_{ij} - \frac{2}{3} k \delta_{ij} \quad (1)$$

where τ_{ij} is the Reynolds stress tensor, ν_T is the turbulent viscosity, ρ is the fluid density S_{ij} is the mean strain-rate tensor, k is the turbulent kinetic energy and δ_{ij} is the Kronecker delta. Given (1) an expression for the turbulent viscosity is needed. The 2006 $k-\omega$ model uses the following relationship for turbulent viscosity:

$$v_T = \frac{k}{\tilde{\omega}}, \quad \tilde{\omega} = \max \left\{ \omega, \quad C_{lim} \sqrt{\frac{2S_{ij}S_{ij}}{\beta^*}} \right\}, \quad C_{lim} = \frac{7}{8} \quad (2)$$

In (2) $\tilde{\omega}$ is the dissipation per unit turbulence kinetic energy, ω is the specific dissipation per unit turbulence kinetic energy and C_{lim} is a constant. The 2006 k - ω model is different from the 1988 k - ω model in that the turbulent viscosity is a function of $\tilde{\omega}$ instead of ω . This change is called the stress-limiter modification which limits the magnitude of the turbulent viscosity when turbulence energy production exceeds its dissipation. The closure coefficients for the 2006 k - ω model are as follows:

$$\alpha = \frac{13}{25}, \quad \beta = \beta_o f_\beta, \quad \beta^* = \frac{9}{100}, \quad \sigma = \frac{1}{2}, \quad \sigma^* = \frac{3}{5}, \quad \sigma_{do} = \frac{1}{8} \quad (3)$$

$$\sigma_d = \begin{cases} 0, & \frac{\partial k}{\partial x_j} \frac{\partial \omega}{\partial x_j} \leq 0 \\ \sigma_{do}, & \frac{\partial k}{\partial x_j} \frac{\partial \omega}{\partial x_j} > 0 \end{cases} \quad (4)$$

$$\beta_o = 0.0708, \quad f_\beta = \frac{1 + 85\chi_\omega}{1 + 100\chi_\omega}, \quad \chi_\omega = \left| \frac{\Omega_{ij}\Omega_{jk}S_{ki}}{(\beta^*\omega)^3} \right| \quad (5)$$

$$\epsilon = \beta^* k \omega \quad \text{and} \quad l = k^{\frac{1}{2}} / \omega \quad (6)$$

In (3)-(6) the closure coefficients α , β , β^* , σ , σ^* , β_o and σ_{do} are all constants with their values provided. The variables ϵ and l in (6) are the specific dissipation rate and turbulence length scale respectively. In (5) the variables f_β , a blending function, and χ_ω , the nondimensional vortex stretching term, are functions of the mean-rotation and mean-strain-rate tensor as well as ω . The mean-rotation and mean-strain-rate tensors are defined as

$$\Omega_{ij} = \frac{1}{2} \left(\frac{\partial U_i}{\partial x_j} - \frac{\partial U_j}{\partial x_i} \right), \quad S_{ij} = \frac{1}{2} \left(\frac{\partial U_i}{\partial x_j} + \frac{\partial U_j}{\partial x_i} \right) \quad (7)$$

where Ω_{ij} and S_{ij} are the mean-rotation and mean-strain-rate tensors respectively. In (7)

U is the velocity in the direction i or j and x is the node location in i or j . Given the

closure coefficients and variables defined by (1)-(7) the equations for turbulence kinetic energy and specific dissipation rate are defined as

$$\frac{\partial k}{\partial t} + U_j \frac{\partial k}{\partial x_j} = \tau_{ij} \frac{\partial U_i}{\partial x_j} - \beta^* k \omega + \frac{\partial}{\partial x_j} \left[\left(\nu + \sigma^* \frac{k}{\omega} \right) \frac{\partial k}{\partial x_j} \right] \quad (8)$$

$$\frac{\partial \omega}{\partial t} + U_j \frac{\partial \omega}{\partial x_j} = \alpha \frac{\omega}{k} \tau_{ij} \frac{\partial U_j}{\partial x_j} - \beta \omega^2 + \frac{\sigma_d}{\omega} \frac{\partial k}{\partial x_j} \frac{\partial \omega}{\partial x_j} + \frac{\partial}{\partial x_j} \left[\left(\nu + \sigma \frac{k}{\omega} \right) \frac{\partial \omega}{\partial x_j} \right] \quad (9)$$

In (8) the left-hand side contains the unsteady turbulence kinetic energy term and the convection term. The right-hand side contains, in order, the production term, dissipation term, molecular diffusion term, and the turbulent transport term. The equation of specific dissipation rate, (9), contains all these same terms and an additional term for the cross diffusion which is the term that is proportional to σ_d . The 2006 k - ω model is fully defined by (1)-(9).

F. Numerical Methods

The simulation was performed using CD-Adapco's CFD code Star-CCM+ [20]. A second-order, implicit unsteady temporal discretization scheme was utilized while spatial discretization was performed using a second-order-accurate scheme which employed the algebraic multigrid (AMG) solver. An unsteady temporal scheme was utilized to capture the time-accurate behavior of the MHK turbine. Also, the coupled flow equation model was selected and compressibility effects of the water were considered. Gradients were computed using the Hybrid Gauss-Least Squares Method. To model the rotation of the turbine Star-CCM+'s Rigid Body Motion (RBM) was used. This method is preferred over other methods including moving reference frame (MRF)

modeling because during the simulation the rotor is physically moving and computational nodes are rotated as well. Also the MRF model is not available for unsteady simulations.

All simulations were carried out on the 272 node Glory cluster at Sandia National Laboratories [22]. Each node consists of four 2.2 GHz quad-core AMD processors with 32 GB of shared memory. All simulations were performed using 10 cores on 10 nodes for a total of 100 cores. The unsteady simulations required approximately 375 cpu-hours depending on the grid size. Simulations, on average took five or more revolutions to reach convergence. The time-step was specified as a function of the rotation rate such that there were 360 time-steps per revolution.

IV. Results

The following simulation was run at the design-point of 5 m/s inflow, 664 RPM and a TSR of 4 to compare with the experimental data [23] obtained with the LDV. To be able to present simulation results with confidence it is necessary to perform a grid sensitivity analysis. Several quantitative assessments of the generated meshes were carried out and include: grid convergence index, apparent order, and Richardson extrapolation. A grid independent solution was reached using the Case 3 mesh and a detailed analysis of the grid sensitivity study used to determine this grid independence is presented below. Comparisons are made for a variety of parameters including, power performance i.e., power, torque, and thrust coefficients, velocity profiles, Reynolds stress, and tower pressure. Additionally, an uncertainty analysis of the experimental data was performed for the power performance coefficients and velocity profiles.

A. Grid Sensitivity

A grid sensitivity study was conducted to determine the effects of increasing the number and density of cells in the general domain, on the rotor and tower, and in the rotor-wake as well as to determine if a grid independent solution could be obtained. As expected with increasing refinement, different flow fields were obtained. Figures 7a-d illustrate the difference in velocity magnitude with the various meshes. The flow parameter that differed the most between the grids was the velocity magnitude in the rotor-wake. For the Case 1 grid (Figure 7a) there were several areas immediately behind the nacelle with low/negative velocity and when compared to the other three grids (Figures 7b-d) this region is much smaller. Additionally, with increased cell count, the

mid-region, rotor-wake velocity tends to increase and begins showing signs of recirculation.

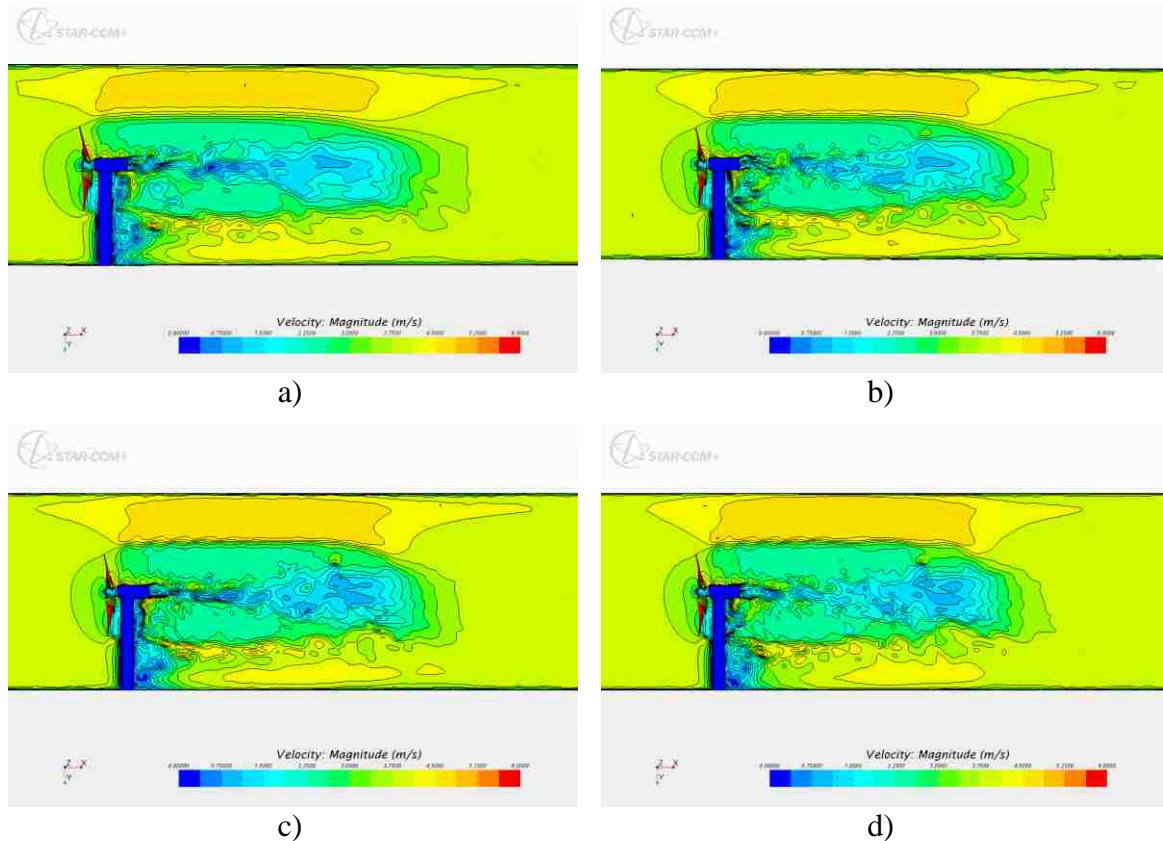


Figure 7: Instantaneous velocity contour plots of a) Case 1, b) Case 2, c) Case 3, and d) Case 4 meshes

Figures 8 and 9 compare the axial velocity profiles at two locations upstream and eight locations downstream of the turbine. As expected, the velocity profiles tend to converge to a single profile with mesh refinement for most cases. The Case 3 and Case 4 meshes produce very similar velocity profiles at most locations suggesting that the prism layer refinement present in the Case 4 mesh did not provide significant improvement to the accuracy of the simulated results of the axial velocity profiles at the given locations. Although not shown the same is true for the Reynolds stress profiles from the Case 3 and Case 4 grids because the refinement was only near the wall.

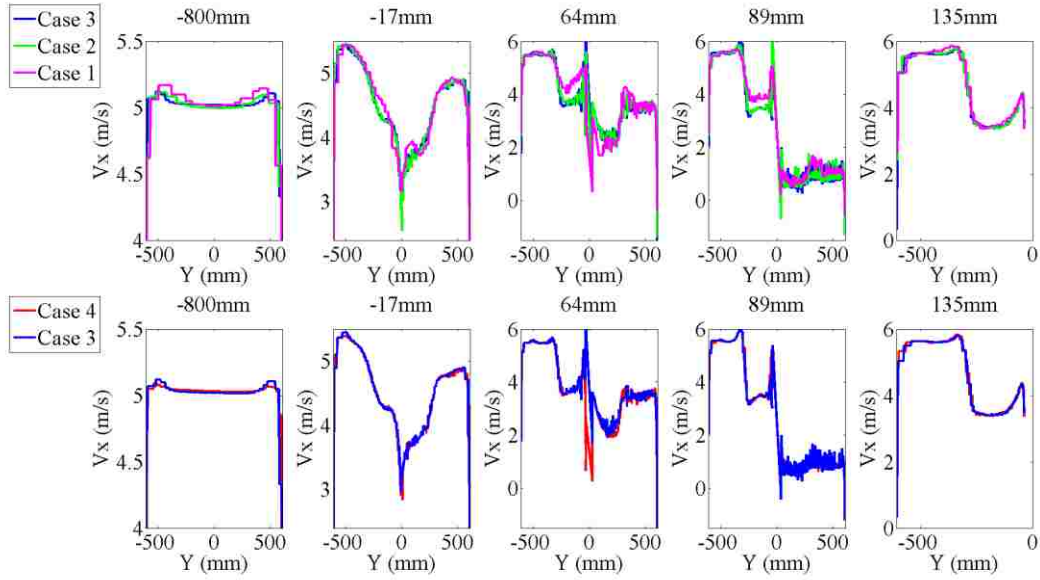


Figure 8: V_x velocity profiles at specified axial locations ($x = -800$ mm to 135 mm, $z = 0$ mm)

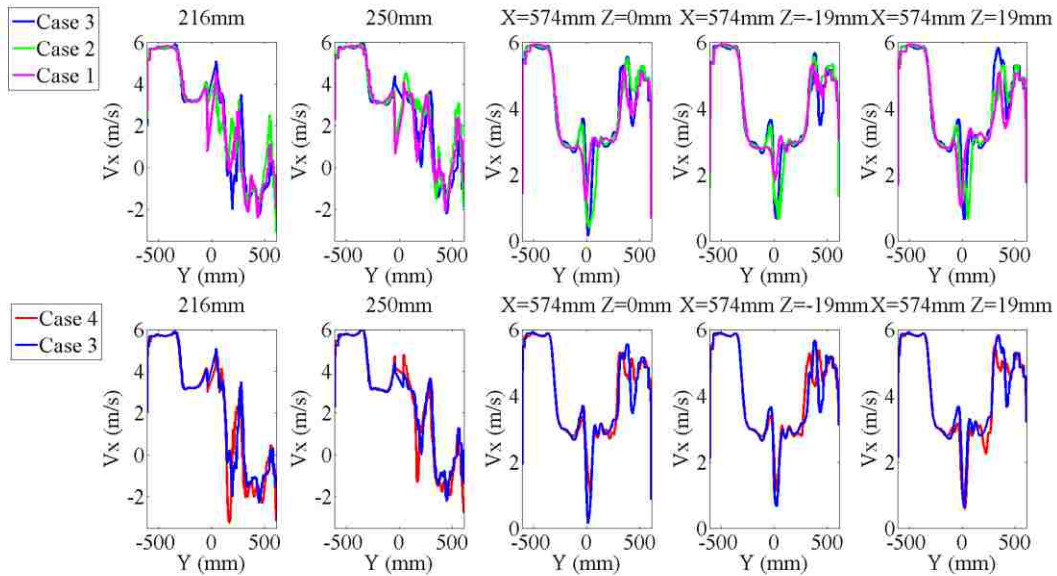


Figure 9: V_x velocity profiles at specified axial locations ($x = 216$ mm to 574 mm, $z = 0$ mm) and $x = 574$ mm, $z = \pm 19$ mm left and right of turbine centerline

Another metric by which to compare the convergence of a mesh is to compare integrated parameters such as the power, thrust, and torque coefficients. Plotting the power coefficient, C_P , torque coefficient, C_Q , and thrust coefficient, C_T , against the number of cells in the mesh, (Figure 10), it is evident that with increasing refinement the

computed values are reaching some level of convergence near the experimentally obtained coefficients although the values do still appear to be rising. For the thrust coefficient, C_T , the simulated values tend toward the experimental values for the Case 1, 2 and 3 grids but diverge for the Case 4 grid. Given this result it is inferred that refining the boundary layer causes a decrement in the accuracy of the integrated parameters most likely due to its influence on the solution near the walls, rotor and tower.

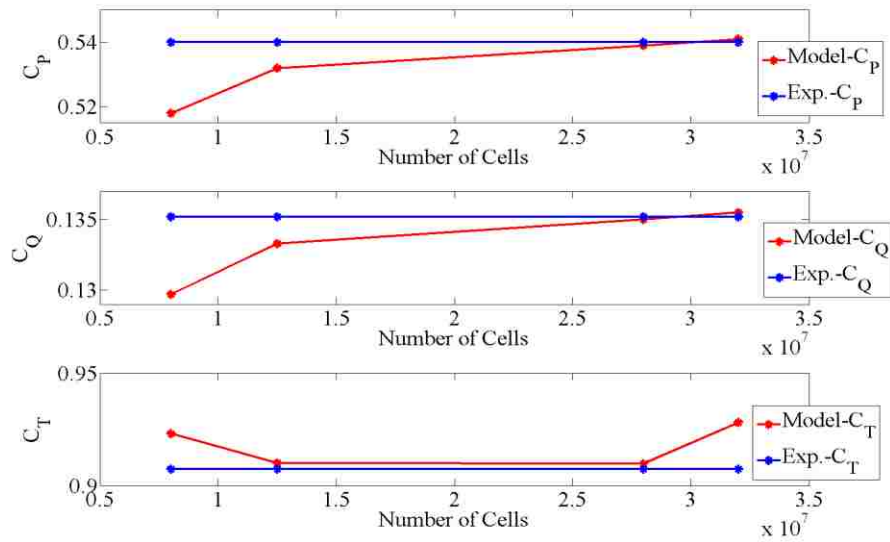


Figure 10: Revolution averaged power, torque, and thrust coefficients obtained through the simulations as a function of the number of cells in the grid compared with experimental data

A well-known metric used to evaluate the legitimacy of solutions obtained on several structured meshes is to use Richardson Extrapolation and determine the apparent order, p , and the grid convergence index (GCI), for the various meshes. Richardson Extrapolation may be used on unstructured grids however the meaning of the results is slightly different as described below. The process of Richardson extrapolation is described in [13] so for the sake of brevity the complete process is not discussed here.

The apparent order, p , is defined as

$$p = \ln\left(\frac{\varphi_{h3} - \varphi_{h2}}{\varphi_{h2} - \varphi_{h1}}\right) / \ln(r) \quad (10)$$

where φ_{h1} , φ_{h2} , and φ_{h3} are a simulated parameter of interest from each of the Case 1, 2, and 3 grids respectively. In (10) the variable r is the refinement ratio between the three grids. To quantify the quality and accuracy of the Cases 1-4 meshes it is essential to determine p and the GCI of the meshes using (10). These values are shown in Table 4. Richardson extrapolation is typically performed on three grids which are increasing in the number of cells thus the Cases 1-3 meshes are considered first and then the Cases 2-4 meshes. The variable, φ_h , used in this grid convergence evaluation is the average coefficient of torque C_Q over the turbine's last, converged, revolution. The relative increase of C_Q from the Case 3 mesh to the Case 4 mesh was 0.37%. The GCI from Case 3 to Case 4 is orders of magnitude larger because the relative difference between the computed torque coefficient from each case, ε_h , is so small. As described in [24] this result is most likely an indication of oscillatory convergence or in very rare cases it is near an exact solution. It is mentioned here that according to [13] for unstructured meshes, p is no longer a metric of order of accuracy but describes the equi-distribution of error if the value of p is large, or signifies that grid refinement is being performed in areas where there is already low error if the value of p is small. Using this information it can be said that the refinement from Case 1 through Case 3 was performed in the proper areas because between those three meshes the apparent order p was equal to 8.2942, which indicates that the error is equally distributed throughout the grid. Conversely, for the refinement that occurred between Cases 2 through 4, the refinement occurred in a region that already had low error which resulted in a low apparent order of 1.3191. Recalling the refinement that occurred between Case 3 and Case 4 the addition of 8 prism layers

resulted in a cell number increase of approximately 4,000,000 cells. Thus, with a low apparent order between the meshes it is inferred that this refinement occurring in an area near the wall was not as crucial to obtaining an accurate solution as the refinement of the rotor, tower, and rotor-wake.

Table 4: Grid Convergence and Apparent Order for Cases 1-4

Case	$\Phi_h(C_Q)$	p	$\varepsilon_h(\varphi_{rh} - \varphi_h)$	GCI	r
Case 1	0.1297	-	-	-	-
Case 2	0.1333	-	0.0036	0.0659%	1.5625
Case 3	0.1350	8.2942	0.0017	0.0012%	2.24
Case 4	0.1355	1.3191	0.0005	2.404%	1.1429

To present the apparent order and GCI results with confidence it is necessary to determine whether or not the generated meshes are within the asymptotic range, meaning that the error scales with the local mesh width. The average mesh width is defined as

$$\bar{h} = \left(\frac{V}{\bar{N}}\right)^{1/3} \quad \text{and} \quad \hat{h} = \left(\frac{V}{\hat{N}}\right)^{1/3} \quad (11)$$

where \bar{h} and \bar{N} are the average mesh width and number of cells in the Case 3 mesh, \hat{h} and \hat{N} are the average mesh width and number of cells in the Case 1 mesh and V is the domain volume. Using (11) the average mesh widths for Cases 1 and 3 were computed. The Case 1 average mesh width was found to be 11.09 mm and the Case 3 average mesh width was 7.3 mm using (11). The global error of a mesh can be computed using the following relationship:

$$\frac{\bar{E}}{\hat{E}} = \left(\frac{\bar{h}}{\hat{h}} \right)^p \quad (12)$$

where \hat{E} and \bar{E} are the global error of the Case 1 and Case 3 grids respectively. The global error (12) is the average numerical error associated with a specific mesh and the error ratio of two grids is useful in determining if the error is within the asymptotic range. The Case 3 mesh is said to be in the asymptotic range if this ratio in (12) trends to zero, meaning a converged solution is being reached with increasing mesh refinement [13]. The apparent order, p , was computed using Richardson extrapolation and was found to be 8.2942, however, before any results are accepted from this extrapolation, the asymptotic range must be confirmed. As mentioned previously a series of grids that are increasing in refinement are said to be in the asymptotic range when the error scales with the local mesh width or when $\frac{\bar{E}}{\hat{E}}$ from (12) trends towards zero. The ratio of global error for Case 3 and Case 1 was computed to be 0.0312 using (12) which confirms the grids are in the asymptotic range.

An additional analysis of value is to determine the required mesh width and number of elements to obtain a near exact solution-the experimental data being the exact solution. To determine the mesh width and number of elements necessary to obtain a near exact solution the constant C from

$$f = F_3 + Ch_3^p \quad (13)$$

must be determined. In (13), f is the experimentally obtained value for the coefficient of torque, F_3 is the value of C_Q for Case 3, and h_3 is the average grid width. Using this equation the constant C can be calculated and it was found to be 1.055×10^{14} . Using this

value for C the global error of the Case 3 mesh, E_3 is computed using the following relationship:

$$h_T \approx \left(\frac{E_T}{E_3}\right)^{1/p} \quad (14)$$

In (14) E_3 is equal to the second term from (13) and was found to be 0.0002. E_T from (14) is the desired error between the simulation and the experimental results and is set to 1×10^{-6} and h_T is the average mesh width necessary to obtain a near exact solution. The number of cells required to obtain a near exact solution is found using the following relationship:

$$N_T \approx \left(\frac{E_3}{E_T}\right)^{3/p} \quad (15)$$

Using (14) and (15), the mesh width and number of cells necessary to obtain a solution that is within 1×10^{-6} of the experimental results can be calculated. The average mesh width for such a solution was calculated to be $0.53h_3$, or 3.8 mm. Similarly, the required number of cells to obtain a solution within 1×10^{-6} of the experimental results was found to be $6.8N_3$, or 190.3×10^6 cells.

Through this analysis it is evident that both the Case 3 and Case 4 meshes are of good quality and accuracy and as such they are suitable to be used in the proposed simulation. The discretization of the mesh is such that it will be able to capture the complex flow and physics that are expected to occur during the simulation. The results presented below were obtained on the Case 3 grid due do the divergence of integrated parameters on the Case 4 grid.

B. Simulation

Parameters such as power performance coefficients, velocity profiles and Reynolds stress profiles are compared to determine how well the CFD simulation was able to capture the complex flow around the Sandia turbine. The simulation results are compared with the experimental data from ARL. The simulation had to meet several criteria before it was said to have a converged solution. To determine if a simulation was converged, residuals were required to have stabilized and reduced by at least three orders of magnitude [25] as well as show convergence of the revolution averaged torque. To perform the averaging of the torque, a trapezoidal interpolation scheme [26] was employed. This was done because in Star-CCM+ only 10,000 points of data are saved and after the simulation passes 10,000 time-steps the time difference between points is irregular especially at earlier times. So, for part of one revolution the data may be output every 0.02 s but for the remainder of the revolution data is shown for every 0.01 s, thus it was necessary to employ an alternative averaging scheme to what may be considered traditional averaging-the sum of all values divided by the number of values. Trapezoidal interpolation is performed using the following equation:

$$T = \frac{1}{2}(b - a)(f(a) + f(b)) \quad (16)$$

The simulation was determined to be converged when the relative difference between the revolution averaged torque of the current and the previous revolution was less than 1% [25]. For the simulation of interest it took five revolutions to reach a relative difference of 0.6%. This means that with a rotation rate of 664 RPM or 69.534 rad/s and a period of 0.0904 s, that the simulation ran for 0.4518 s. The time-step size was selected

by defining it as a function of rotational speed with 360 time-steps per revolution being sufficiently small for this unsteady simulation. With 360 time-steps per revolution, 5 iterations per time-step and a time-step of 0.000314s, the simulation had a total of 9000 iterations.

1. Power Performance

A metric used in this report to determine the CFD simulation's ability to accurately predict the flow around the Sandia turbine is how well the power performance results compare to the experimental data. There are several data sets to choose from but dataset Sandia_3496 [23] maintained the most consistent RPM and inflow conditions, thus it is best suited, to use in comparing simulation data. It is worthwhile to mention how Star-CCM+ computes the torque, power and thrust because it may lend insight into potential sources of error and uncertainty. Star-CCM+ uses the following equation to compute thrust:

$$T = \int \rho \mathbf{v} \mathbf{v} \cdot d\mathbf{s} + \int (p - p_{atm}) d\mathbf{s} \quad (17)$$

The thrust is computed using (17), where ρ is the fluid density, \mathbf{v} is the fluid velocity vector, $d\mathbf{s}$ is the integrated surface, p is the pressure on the integrated surface and p_{atm} is the atmospheric pressure. The values for ρ , \mathbf{v} , p , and p_{atm} were taken from the simulation near the blade surface. Star-CCM+ calculates the thrust by integrating the momentum flux and pressure force over a specified boundary or derived part. Only the thrust component in the x-direction is used in the following comparisons. Additionally, to compute the torque in Star-CCM+, a moment report must be created and the moment arm specified which was set to the radius of the turbine. The surface of the blades is used in the pressure calculation which in turn is used for the moment computation. In simplified

terms, by computing the force on the blades and multiplying by distance, the torque is obtained. The power is computed in a Matlab [27] script by taking advantage of the following relationship:

$$P = \omega Q \quad (18)$$

In (18) P is the power, Q is torque, and ω is the angular frequency of the turbine.

The power performance data is presented in Figures 11-13. All power performance data is presented as non-dimensionalized power coefficients and are computed using the following equations:

$$C_P = P / \frac{1}{2} \rho A V_\infty^3 \quad (19)$$

$$C_T = T / \frac{1}{2} \rho A V_\infty^2 \quad (20)$$

$$C_Q = Q / \frac{1}{2} \rho A R V_\infty^2 \quad (21)$$

In (19)-(21) P , T , and Q are the calculated power, thrust and torque respectively, A is the frontal area of the turbine, R is the radius of the turbine and V_∞ is the upstream velocity.

The torque coefficient over the last revolution of the simulation is compared to experimental data in Figure 11. This plot illustrates how the torque coefficient varies with turbine rotor rotation angle. The simulation under predicts the peaks and troughs of the experimental data but they are nearly in phase. The three distinct dips in the C_Q curve are caused by blade-tower interaction. As each of the three blades passes the tower in the experiment and simulation there is unsteady loading on the assembly. In the experiment this behavior manifests itself as an unsteady load on the driveshaft [8]. The blades pass the tower every 120° as noted by the drop in torque at 0° , 120° , and 240° . There is a slight difference in where the blade passes the tower for the simulation as compared to

the experiment however, this may be related to a slight difference in experimental and simulated rotation rate.

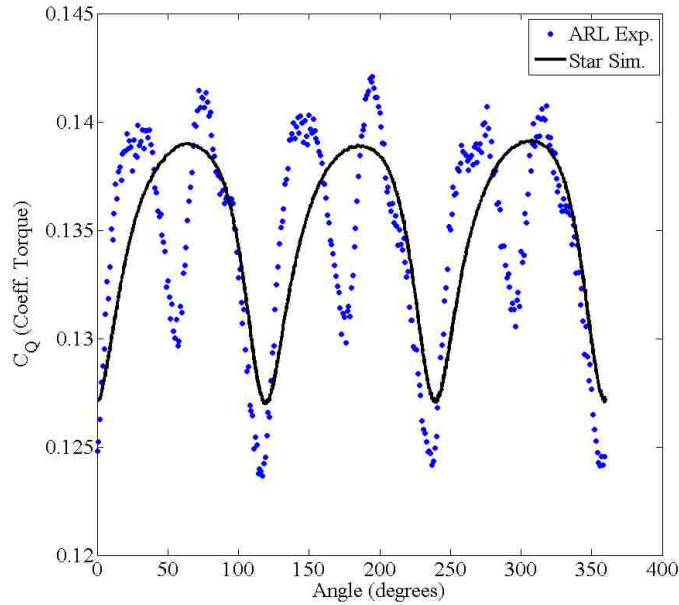


Figure 11: Single revolution torque coefficient history of simulation and time-averaged experimental data

The simulation was able to accurately capture the behavior of the rotating turbine with slight differences in the minimum and maximum torque coefficients and blade-tower passing phase. The secondary dips in performance seen at approximately 50° , 170° , and 290° are most likely due to the lift loadings of one blade relative to the other two. As one blade passes the tower the other two blades experience lift which may have caused a drop in performance measured by the sensors on the driveshaft but this phenomena was not captured by the simulation. The relative difference of the revolution averaged torque coefficient for the simulation is -0.201% as noted in Table 5.

Table 5: Revolution averaged power performance coefficients and relative difference compared to experimental values

Name	C_Q	C_T	C_P
Case 3	0.1350	0.9097	0.5389
Experiment	0.1347	0.9073	0.5378
Relative Difference (%)	0.201%	0.265%	0.201%

Similar to Figure 11, Figure 12 compares the thrust coefficient histories over one revolution for the simulation and experiment. As with the torque coefficient comparison there is good agreement between the simulation and experiment for the reduction in thrust due to blade tower interaction. However, the simulation does over-predict the peak thrust coefficient values at 50° , 170° , and 290° , which is where the secondary dips in performance are seen. As mentioned previously the cause of this is likely the lift loading of one blade relative to the other two. From Table 5 the relative difference in the revolution-averaged thrust coefficient between the Case 3 simulation and experiment is - 0.265%, where the simulation computed a revolution averaged thrust coefficient of 0.9097 and from experimental data C_T was found to be 0.9073.

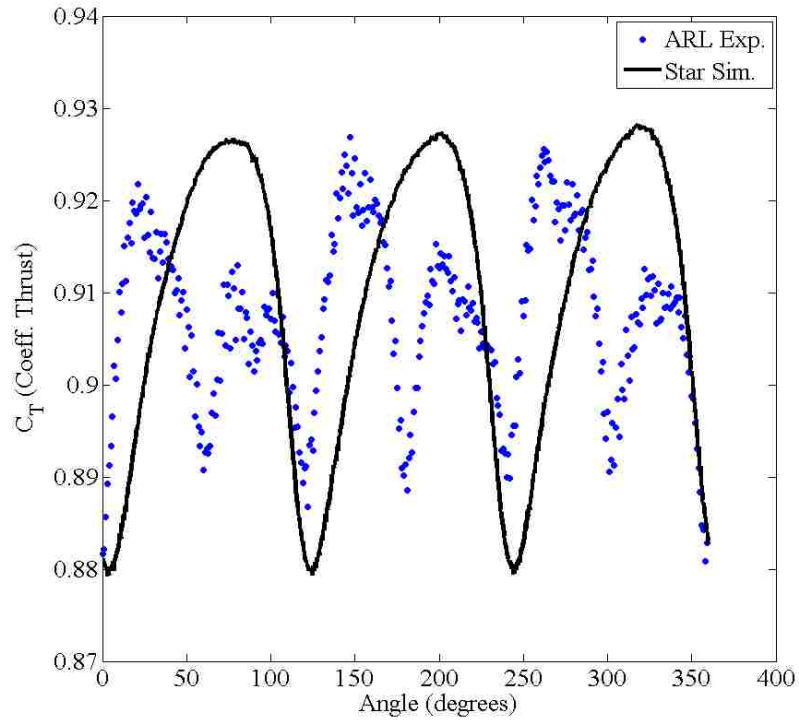


Figure 12: Single revolution thrust coefficient history of simulation and experimental data

The power coefficient, C_P , comparison (Figure 13), depicts the same behavior as the torque coefficient plot. This result is due to the relationship described by (18), where the power is simply computed as the product of the torque and angular frequency. The same behavior as that described for the torque coefficient comparison is applicable here. The relative difference in the revolution averaged power was -0.201%, where the experimental power coefficient was 0.5378 and the simulation C_P was equal to 0.5389.

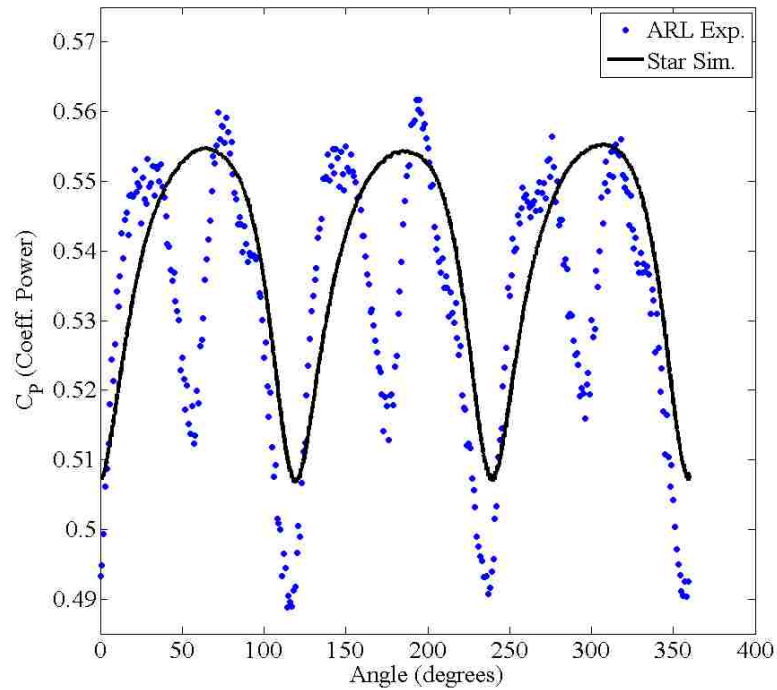


Figure 13: Single revolution power coefficient history of simulation and experimental data

In comparing the converged revolution simulation data with the experimental data it is evident that the CFD model was able to accurately capture the majority of the behavior seen in the experimental data. However, there were some differences. The simulation under predicted both the minimum and maximum torque and power coefficients and conversely the simulation over predicted the minimum and maximum thrust coefficient. Even though there are some discrepancies between the single revolution power performance history, the revolution averaged coefficients had reasonable agreement, with no more than 0.265% difference between the simulation and experiment. For general research and industry applications the revolution averaged power performance may be sufficient for prototype design, which makes a strong case for CFD simulations to replace or at least supplement expensive laboratory experiments.

2. Velocity Profiles

To assess the accuracy of the simulation results, the axial (V_x) and radial (V_z) velocity profiles were compared to experimental data. In the experiment, LDV velocity data was collected at ten locations along the tunnel. Eight locations were downstream of the turbine and two upstream. All but two of the measurement locations were in line with the centerline of the turbine and these two locations were one diameter downstream (574 mm) and offset 19 mm in either direction of the centerline. The experimental setup is shown in Figure 14 which was taken from [8]. The survey numbers from Figure 14 that simulation results were compared to are 5, 8, 20, 21, 3, 11, 13, 16, 17, and 18. Surveys 17 and 18 are the two surveys that were offset by 19 mm from the centerline. The locations of the surveys are shown in Table 6. All axial locations are given relative to the nose cone leading edge where upstream is negative and downstream is positive x -direction. An important insight is that the experimental data was only collected at discrete transverse locations across the tunnel. The simulation data was obtained for the entire cross-section, however, to make an accurate comparison between the two datasets, the simulation data is presented in the confines of the experimental data range. The positive transverse locations are referred to as the tower side while negative transverse locations are described as the console side.

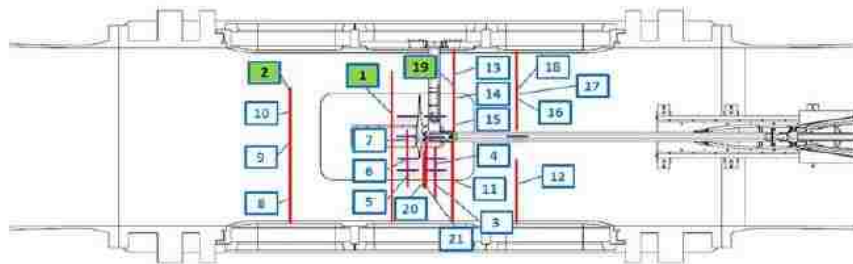


Figure 14: ARL experimental setup and measurement locations for flow field quantification [8]

Table 6: Survey locations for flow field LDV measurements

LDV Survey No.	Axial location (mm)
3	135
5	-17
8	-800
11	216
13	250
16	574
17	574 (19 mm above centerline)
18	574 (19 mm below centerline)
20	64
21	89

The velocity profile comparisons are made in Figures 15 and 16. Figure 15 compares the axial velocity computed by the simulation with the experimental data. Beginning with the velocity profile at -800 mm it is evident that the experiment had a nearly uniform velocity distribution upstream of the turbine at the transverse measurement locations. The simulation has an inverse parabolic shape with values near the experimental data but the inlet profiles were not identical. At $x = -17$ mm, just in front of the turbine, the simulation predicts a drastic drop in velocity near the centerline while the console side has an increase in velocity from the prescribed inlet velocity of 5 m/s. The experimental data shows the same trend but does not show the same centerline velocity deficit as the simulation results. The velocity profile comparisons for 64 mm, 89 mm, 135 mm and 216 mm show good agreement between experimental data and simulation results. The velocity on the console side is high and conversely the velocity is low, compared to the inlet velocity, on the tower side for both the experiment and simulation. This behavior is expected because the tower obstructs the flow, causing a decrease in velocity, while the console side is comparatively open, thus a high velocity. The simulation velocity data at

250 mm does not agree with the experimental data. The reason for this is that there is a large amount of uncertainty in the data and a more detailed discussion of the uncertainty in the experimental data is given in the sub-section 5. *Experimental Uncertainty*. Comparisons between experimental and simulation results at 574 mm and at 574 mm, 19 mm above and below the centerline show fair agreement. However, for $x=574$ mm at $z = -19$ mm and $x=574$ mm at $z = 19$ mm, the simulation predicts a drop in velocity at approximately $y=400$ mm and the experimental data does not exhibit the behavior. For all but a few circumstances whose deviations were explained the simulation was able to accurately calculate the axial velocity profiles at the described locations.

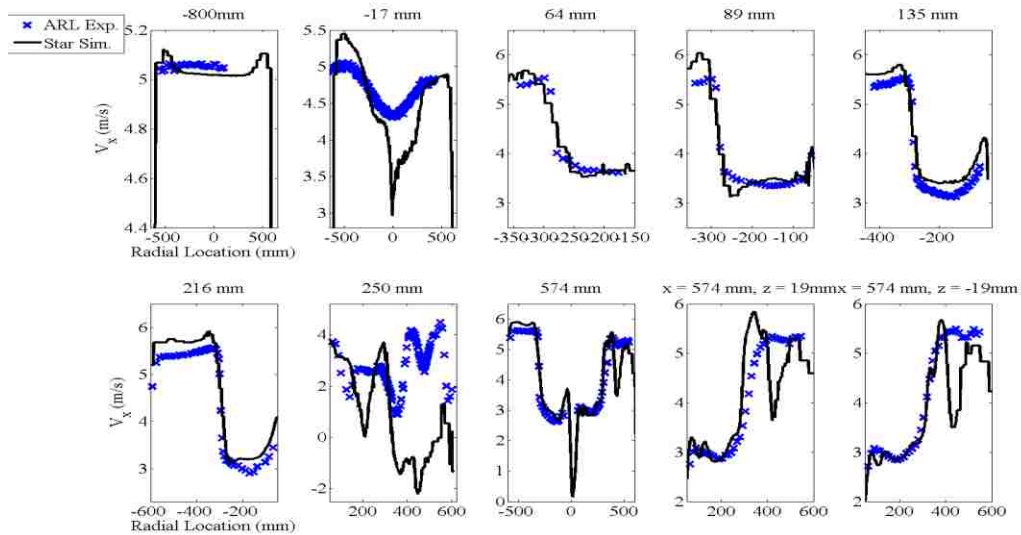


Figure 15: V_x velocity profiles at specified axial and tangential location ($z = 0$ mm unless specified otherwise) for simulation and experimental data

The radial velocity profiles from the simulation are compared to the experimental data in Figure 16. As with the axial profiles the radial profiles show good agreement at 64 mm, 89 mm, 135 mm and 216 mm downstream of the turbine. The simulation accurately captures the radial velocity deficit due to the turbine obstructing flow in the tunnel. Of note is the near exact agreement between experimental and simulation results

seen at 135 mm and 216 mm. At the inlet, $x = -800$ mm, the radial velocity computed by the simulation agrees well with the experimental data. The simulation predicts a nearly uniform, 0 m/s, radial velocity profile which is in concordance with the experiment. At -17 mm the simulation predicts a spike in velocity at the centerline of the turbine, however, the experimental data shows a steady decrease in radial velocity from the console side to the tower side. The centerline velocity profile at 574 mm had very good agreement with experimental data from approximately $y = -600$ mm to 0 mm, which lies on the console side of the tunnel. Near the center of the tunnel the simulation predicts a jump in radial velocity followed by various spikes. The simulation results suggest that there is a discontinuity in the solution from $y = 0$ mm to 50 mm, with the experimental data showing a steady profile while the simulation predicts a spike in the radial velocity. The remaining two surveys, $x = 574$ mm and $z = \pm 19$ mm, correspond well with one another especially on the console side of the tunnel though near the centerline the experimental and simulation results do not agree well.

Overall, the simulation was able to accurately predict the behavior of the velocity profiles. The survey points that disagreed most were at -17 mm and 250 mm. It is apparent from computing the uncertainty related to the experiment that the data at 250 mm has substantially more error than velocity measurements at other locations. A partial explanation is suggested in [8] where, this peculiar behavior is believed to be associated with a combination of near wall junction flow and window assembly.

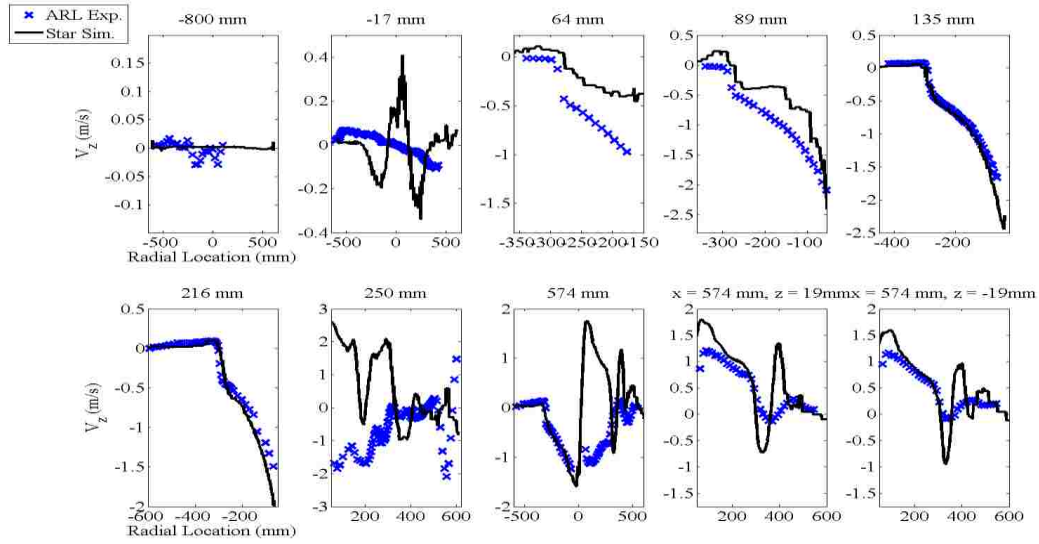


Figure 16: V_z velocity profiles at specified axial and radial location ($z = 0$ mm unless specified otherwise) for simulation and experimental data

3. Reynolds Stress

Velocity variance is a statistical measurement of the Reynolds stress present in a given flow. Using the LDV velocity data and ARL's in-house algorithm, the velocity variance at the locations described in Table 6 was computed. For a detailed description of the meaning of velocity variance and how ARL calculated it using their measurement equipment see [8]. The figures presented below compare the axial Reynolds stress (τ_{11}) and radial Reynolds stress (τ_{33}) between the simulation results and experimental data. Reynolds stresses stem from momentum transfer by the fluctuating velocity field [28]. In a physical sense the Reynolds stress, denoted τ_{ij} , is the momentum flux of the i^{th} component in the j^{th} direction caused by the fluctuating velocity field [29]. It is useful to view Reynolds stress plots because they bring insight to the transport of momentum through the flow which in turn helps visualize what effect the rotating turbine has on the mean flow. To compare the simulated Reynolds stresses computed using (1), with the

experimental velocity variance the experimental data must be multiplied by the fluid density. The resulting equation for experimental Reynolds stress is $\tau_{ij} = \rho \overline{u'_i u'_j}$ where axial velocity variance is $\overline{u'u'}$ and radial velocity variance is $\overline{w'w'}$.

The axial Reynolds stress for the given measurement locations is provided in Figure 17. As expected, there is very little Reynolds stress for the inlet portion of the tunnel, -800 mm and -17 mm. As the flow progresses downstream past the turbine there is a large peak in the Reynolds stress at approximately -290 mm which coincides with the radius of the turbine blade (287.4 mm). This peak is likely caused by the tip vortices shed from the turbine blade as it rotates. Similarly, at all other downstream locations there is a peak in the axial Reynolds stress which occurs at the same location but decays in magnitude downstream of the turbine. Again, the simulation reveals good agreement of the Reynolds stress with experimental data at -800 mm and -17 mm where the value is constant and nearly zero.

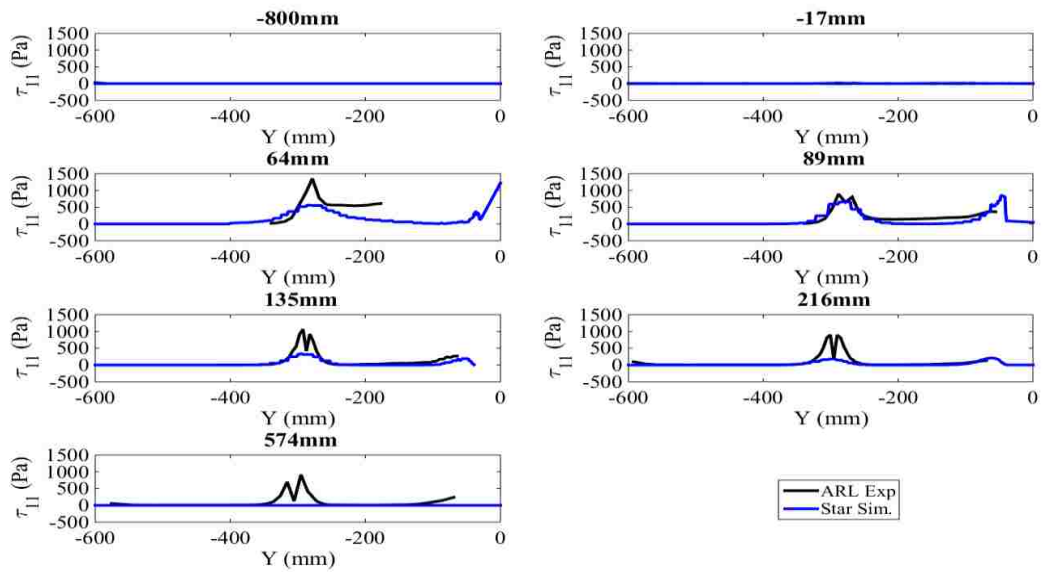


Figure 17: Axial Reynolds stress profiles at specified locations for simulation and experimental data

At 64 mm downstream of the rotor there is a large peak in the Reynolds stress and the simulation shows that there is an increase in the Reynolds stress at this location but it is half the magnitude seen in the experimental data. Moving downstream to 89 mm there is fair agreement between the two methods with the simulation predicting the same location and magnitude of axial Reynolds stress as the experiment. Further downstream at 135 mm, 216 mm and 574 mm the simulation correlates well with the experiment except for the peak Reynolds stress at -290 mm. There is a distinct decay in the magnitude of the Reynolds stress for the simulation data as the flow moves downstream and at 574 mm the simulation predicts near zero Reynolds stress, a behavior contradicting the experimental data which still shows strong stresses up to 574 mm. A detailed view of the axial Reynolds stress for 64 mm, 135 mm, 216 mm and 574 mm is provided in Figure 18.

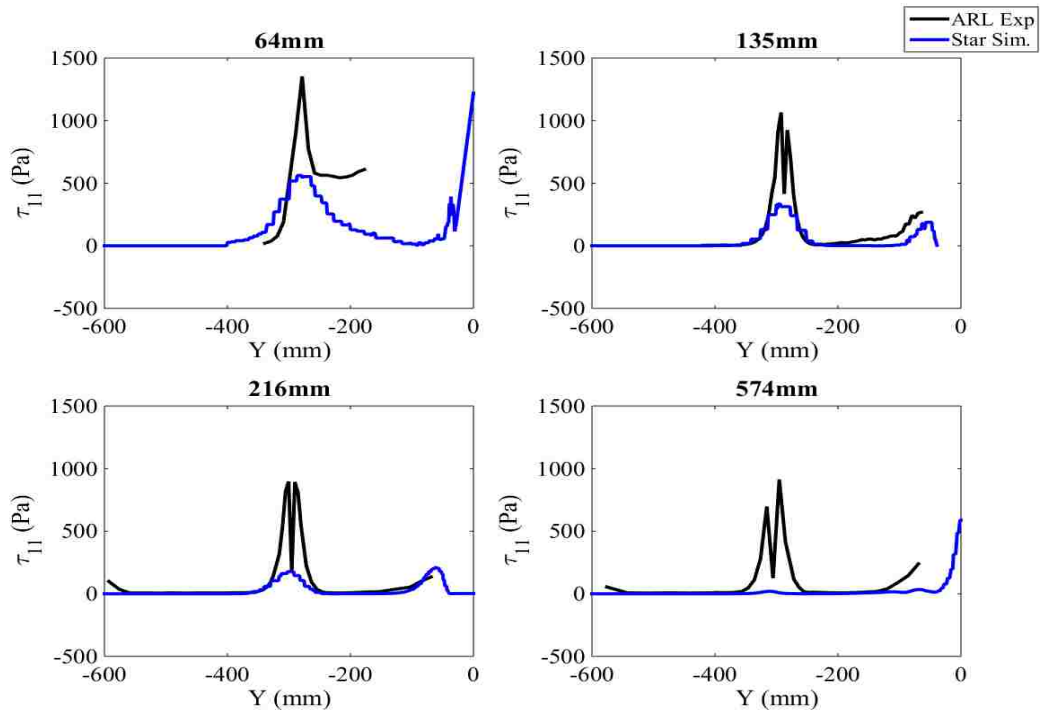


Figure 18: Axial Reynolds stress detail picture for $x = 64$ mm, 135 mm, 216 mm, and 574 mm downstream of turbine

The reason for this discrepancy is likely due to the 2006 $k-\omega$ turbulence model's numerical schemes. Some turbulence models numerical schemes, including those of the 2006 $k-\omega$ model have been found to be too diffusive which results in a high eddy viscosity. This highly diffusive behavior is particularly dominant in areas where the strain rate is influenced by rotation [30], which surely occurs in the simulation. The latest version of the $k-\omega$ model contains a stress limiter relation which limits the production of kinetic energy when it exceeds the dissipation. This stress limiter term could cause the model to under-predict the downstream Reynolds stress, due to the tip vortices, because the turbulent kinetic energy is limited thus reducing the computed Reynolds stresses. In future work it would be beneficial to alter this stress limiting term to allow more turbulent kinetic energy, thus allowing a lower eddy viscosity in the vortex core which may lead to more realistic and accurate stress values. The radial Reynolds stress of the simulation is compared to the experimental data in Figure 19. As with the axial Reynolds stress, there is good agreement between the simulation and experiment at -800 mm, -17 mm, and 89 mm.

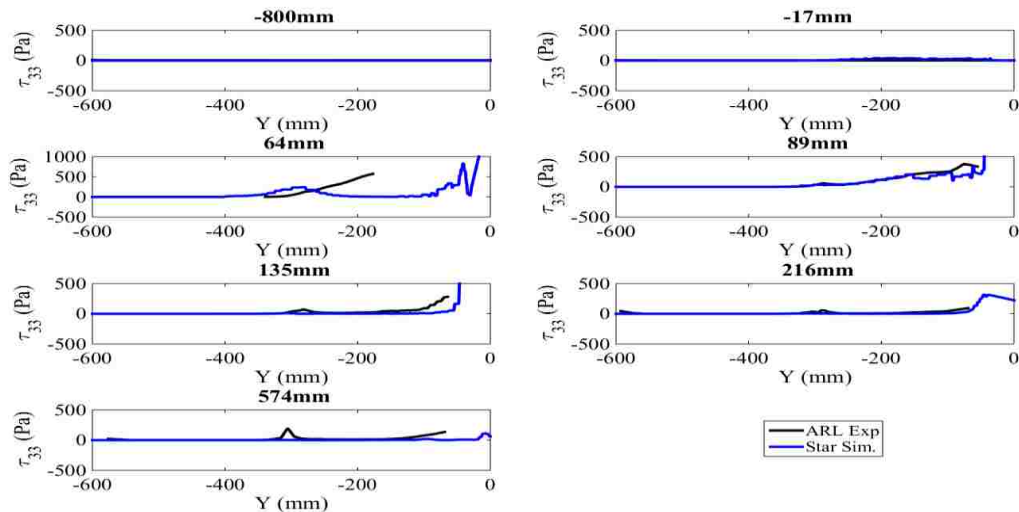


Figure 19: Radial Reynolds stress at specified axial locations for simulation and experiment

Although there appears to be good agreement at 64 mm, 135 mm, 216 mm, and 574 mm, if the axis scaling is changed, as in Figure 20, it is evident that the simulation was unable to predict the peaks of radial Reynolds stress which occur near -290 mm.

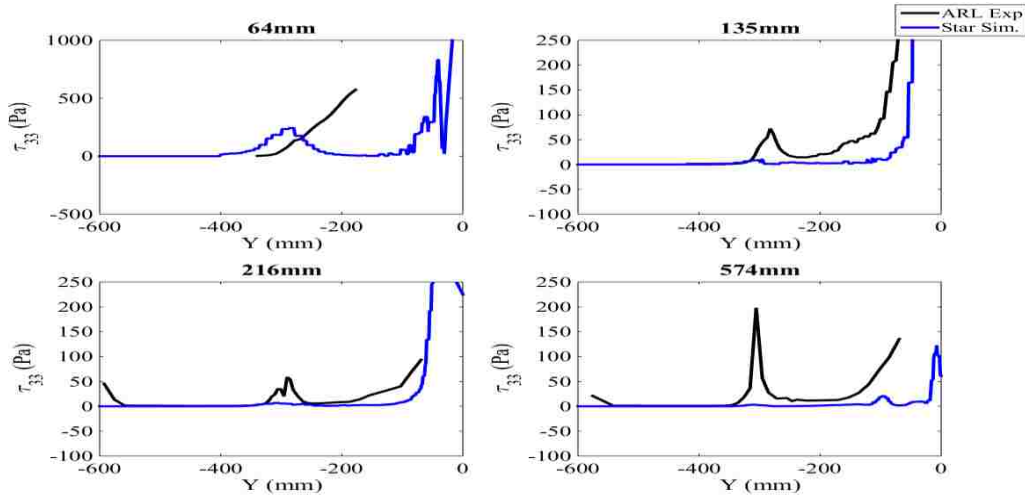


Figure 20: Radial Reynolds stress detail picture for $x = 64$ mm, 135 mm, 216 mm, and 574 mm

As stated previously, this is most likely due to the turbulence model's inability to preserve the turbulent kinetic energy due to its numerical scheme thus the Reynolds stress at these downstream locations is dissipated. The simulation does, however, predict the after peak Reynolds stress well showing that it increases near the centerline.

Good agreement was achieved between the simulation and experiment for both axial and radial Reynolds stress. Particularly good agreement occurred at upstream locations of -800 mm and -17 mm and at the downstream location of 89 mm. In other locations the general behavior of the Reynolds stress was predicted and agreed well with the experimental data but the simulation was unable to predict the peaks in Reynolds stress which occurred near the location of expected tip vortices. Modifications to the 2006 $k-\omega$, as described previously may improve the model's ability to predict these downstream Reynolds stresses. The simulation's ability to predict the general behavior of the

Reynolds stress of the flow field should further encourage the use of CFD as a tool for modeling current-driven MHK turbines.

4. Unsteady Tower Pressure

The next parameter for analysis is the unsteady tower pressure with simulation data compared to experimental data. The following comparison uses the pressure coefficient:

$$c_p = \frac{p - p_\infty}{\frac{1}{2}\rho_\infty V_\infty^2} \quad (22)$$

In (22) p_∞ is the freestream pressure and ρ_∞ is the freestream density.

Experimental data is available for many locations along the tower though only comparisons at 40%, 70%, 100% and 110% of the turbine blade span were made because they are believed to be the most crucial locations to understanding the unsteady tower pressure. These locations correspond to 114.84 mm, 200.97 mm, 287.4 mm and 315.81 mm on the tower measured downwards from the centerline of the turbine. Unsteady tower pressure is important to the design of turbines and their support structure because it gives insight to the cyclic loads the tower will experience due to the blades passing the tower and tip vortices that are shed and impinge upon the tower. Furthermore, it is important to characterize unsteady tower pressure as it may cause vibration and noise.

The unsteady tower pressure at 40%, 70%, 100% and 110% of blade span as calculated by the simulation and recorded during the experiment are compared in Figure 21. For all four locations it is evident that the simulation was able to predict the peak pressure coefficient that occurred at approximately 0° , 120° , and 240° which coincide

with the turbine blade passing the tower. From this comparison it is apparent that the tower pressure can be seen as a function of blade span because at different locations along the tower, different pressures are experienced due to the blade geometry and how flow is projected from the trailing edge of the blade as well as the influence of tip vortices on tower pressure.

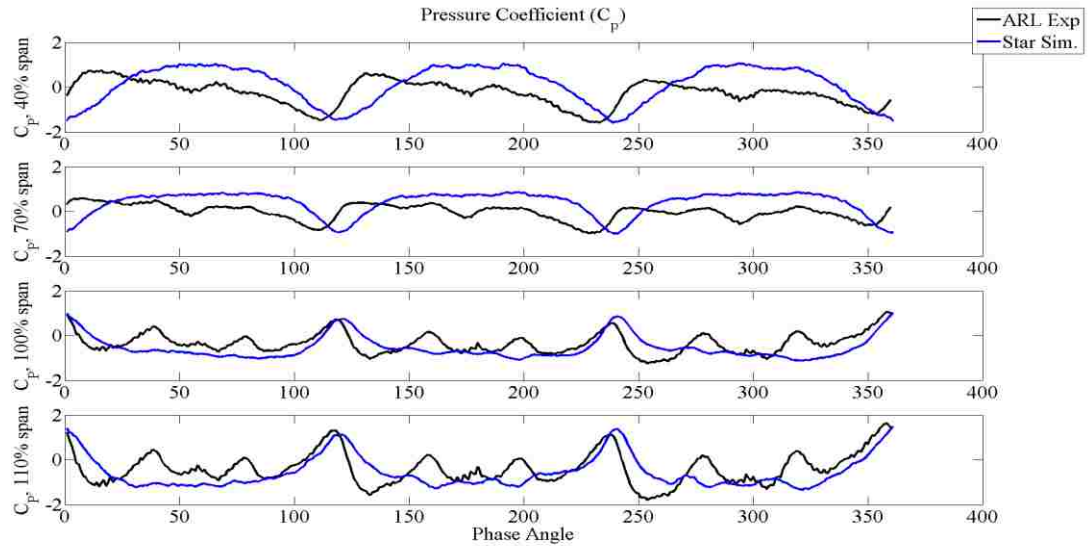


Figure 21: Tower pressure coefficient at specified radial positions along tower for simulation and experimental data. Distance is specified as percentage of turbine blade span.

At 40% blade span the simulation results agree well with the experimental data especially for the drops in pressure associated with the blade-tower interaction. The simulation slightly over predicts the pressure in the central region of the cyclic pressure loading which occurs at approximately 50° , 170° , and 290° . Similar to the comparison made at 40% blade span, at 70% blade span the blade-tower interaction pressure predicted by the simulation agrees well with the experiment while still over-predicting the pressure in the central region as described above. At 100% blade span the simulation has very good agreement with experimental data. From the experimental data it is apparent that there is more cyclic pressure experienced at this location which is explained by predicted shed

vortices impinging on the surface of the tower. The vortices are not present at 40% and 70% because these locations are too far inboard on the rotor blade to have any significant shed vortices. The pressure coefficient comparison at 110% blade span shows near exact agreement between the simulation and experiment except for the aforementioned cyclic pressure loading seen in the experiment.

The simulation was able to closely predict the unsteady tower pressure experienced during the experiment except for the changes in pressure at 100% and 110% of blade span. With good agreement between experimental data and simulation results it is evident that CFD may be used to predict unsteady tower pressure and by extension the cyclic loading on the tower due to blade-tower interaction.

5. Experimental Uncertainty

In comparing the simulation results with the experimental data it is beneficial to determine the uncertainty associated with the experimental data. For a complete description of the post-processing and uncertainty analysis performed by ARL on the experimental data see [8]. The uncertainty associated with the calculated power performance coefficients, axial velocity, and radial velocity is discussed below.

The experimental dataset provided by ARL contains the computed standard deviation associated with each variable of interest. For determining the uncertainty associated with the power performance the variables of interest are torque, thrust, density, rotation rate, and freestream velocity. The standard deviations associated with these flow parameters were obtained from the ARL dataset. To compute the uncertainty associated

with torque, thrust and power coefficients it is necessary to use the standard deviation equation for non-linear combinations [31]:

$$\sigma_f^2 = \left| \frac{\partial f}{\partial x} \right|^2 \sigma_x^2 + \left| \frac{\partial f}{\partial y} \right|^2 \sigma_y^2 + \left| \frac{\partial f}{\partial z} \right|^2 \sigma_z^2 + \dots + \left| \frac{\partial f}{\partial n} \right|^2 \sigma_n^2 \quad (23)$$

For ease of calculation, the simplified version for computing the standard deviation for non-linear combinations, which ignores correlations and assumes independent variables, is used (23). Using (23), the variance of the torque coefficient may be computed as

$$\sigma_{cQ}^2 = \left| \frac{\partial f}{\partial Q} \right|^2 \sigma_Q^2 + \left| \frac{\partial f}{\partial v_{inf}} \right|^2 \sigma_{v_{inf}}^2 + \left| \frac{\partial f}{\partial \rho} \right|^2 \sigma_\rho^2 \quad (24)$$

In (24), the equation for the thrust coefficient, (21), is used. Performing the differentiation of (21), with respect to the specified variables as described by (24), the equation for the standard deviation of the torque coefficient is found to be

$$\sigma_{cQ}^2 = \left(\frac{1}{0.5 * Area * R} \right)^2 * \left(\left| \frac{1}{V_{inf}^2 * \rho} \right|^2 \sigma_Q^2 + \left| \frac{-2 * Q}{V_{inf}^3 * \rho} \right|^2 \sigma_{v_{inf}}^2 + \left| \frac{-Q}{V_{inf}^2 * \rho^2} \right|^2 \sigma_\rho^2 \right) \quad (25)$$

In a similar fashion, the equation for the uncertainty associated with the thrust coefficient was found to be

$$\sigma_{cT}^2 = \left(\frac{1}{0.5 * Area} \right)^2 * \left(\left| \frac{1}{V_{inf}^3 * \rho} \right|^2 \sigma_T^2 + \left| \frac{-3 * T}{V_{inf}^4 * \rho} \right|^2 \sigma_{v_{inf}}^2 + \left| \frac{-T}{V_{inf}^3 * \rho^2} \right|^2 \sigma_\rho^2 \right) \quad (26)$$

and the uncertainty associated with the power coefficient is

$$\sigma_{cP}^2 = \left(\frac{1}{0.5 * Area} \right)^2 * \left(\left| \frac{\omega}{V_{inf}^3 * \rho} \right|^2 \sigma_Q^2 + \left| \frac{-3 * \omega * Q}{V_{inf}^4 * \rho} \right|^2 \sigma_{v_{inf}}^2 + \left| \frac{-\omega * Q}{V_{inf}^3 * \rho^2} \right|^2 \sigma_\rho^2 + \left| \frac{Q}{V_{inf}^3 * \rho} \right|^2 \sigma_\omega^2 \right) \quad (27)$$

It is necessary to formulate (25)-(27) because the uncertainty in the base flow parameters, i.e., velocity, density, thrust, torque, and rotation rate propagate through the equations that are used to compute the power performance coefficients.

Figures 22-24 illustrate the uncertainty associated with the experimental data for the power performance coefficients and how the simulation results compare to the experiment in terms of this uncertainty. The uncertainty data is available for all points in the experiment but for simplicity only every tenth uncertainty error bar is plotted. Additionally, the presented error bars for the torque, thrust and power coefficients are equivalent to plus and minus the square root of (25)-(27), respectively.

Figure 22 displays the simulation torque coefficient data compared with the experimental data and corresponding error bars. It is evident that on average the experimental data has an approximate uncertainty of 5%. The simulation calculated torque coefficient falls within the shaded error area except the secondary dips seen at 50°, 170° and 290°. This behavior indicates that the simulation data has fair agreement with the experimental data. Also, the fact that the simulation data does not fall within the error associated with the secondary dips suggests that the experiment was able to capture some physical behavior that the CFD simulation was not able to.

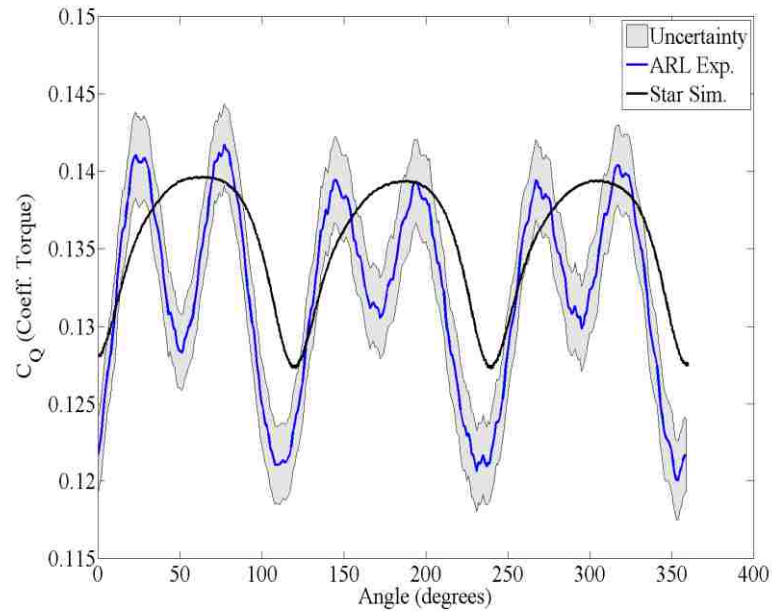


Figure 22: Single revolution torque coefficient history for simulation and experiment with error in grey

The thrust coefficient had approximately a 3% relative error associated with the experimental data. The simulation data compared with experimental uncertainty is shown in Figure 23. As with the previous comparison for the torque coefficient, for the thrust coefficient most of the simulation data points fall within the experimental uncertainty except for the secondary dips. As mentioned previously these secondary dips in performance are likely due to periodic loading of one blade relative to the other two.

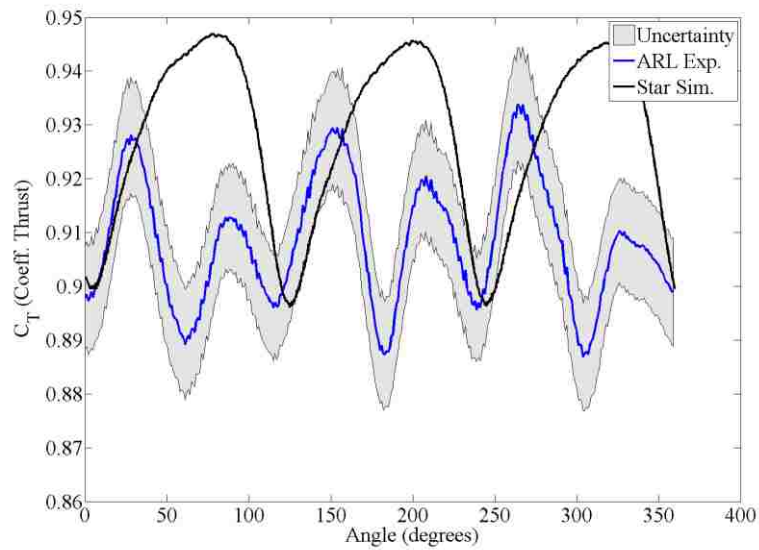


Figure 23: Single revolution thrust coefficient history for simulation and experiment with error in grey

Figure 24 depicts the relation between simulation results and experimental uncertainty for the computed power coefficient. As with the other performance coefficients, the power coefficient shows good agreement with experimental results. Quantifying the uncertainty associated with the performance coefficients of the Sandia turbine illustrates the simulation's ability to accurately predict the performance and how it falls within the experimental uncertainty.

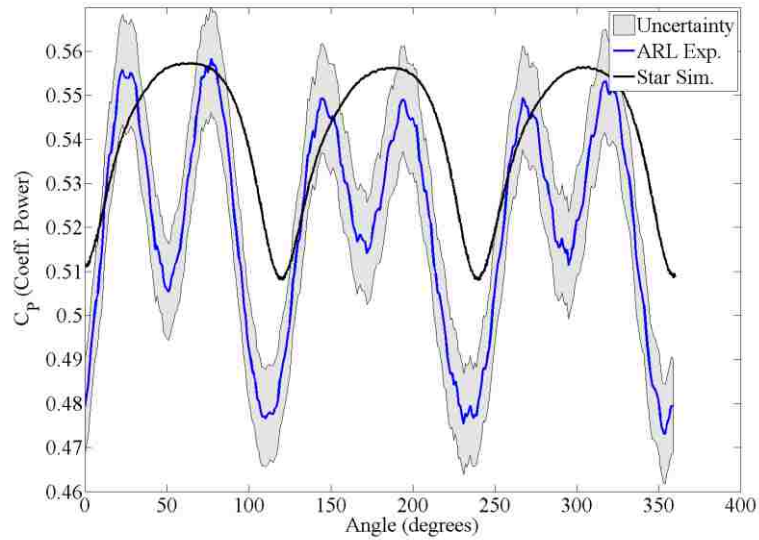


Figure 24: Single revolution power coefficient history for simulation and experiment with error in grey

Figures 25-29 compare the simulation results with the uncertainty associated with the experimental axial and radial velocity profiles. As discussed in the sub-section *Velocity Profiles*, the simulation was able to correctly predict the velocity profiles for the various measurement locations. At -800 mm (Figure 25) the simulation results are within the radial velocity uncertainty for all transverse locations. The axial and radial velocity profiles for -17 mm (Figure 25) still do not show the desired accuracy of simulation results compared to the experiment even when considering the experimental uncertainty.

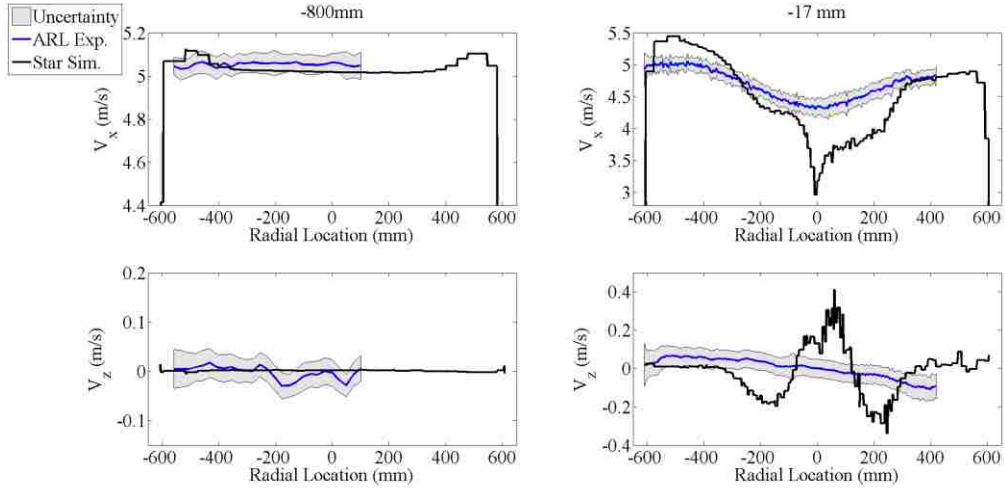


Figure 25: V_x and V_z velocity profiles with error in grey on experimental data for $x = -800$ mm and -17 mm

The velocity profiles, both axial and radial, for 64 mm and 89 mm do show reasonable agreement with the experimental data. When considering the uncertainty in measurements the simulation data is seen to correctly calculate the velocity profiles for both these locations. Most simulation values fall within the experimental error for these measurement locations (Figure 26). Similarly, for 135 mm and 216 mm (Figure 27) the majority of the computed results lie within the experimental uncertainty.

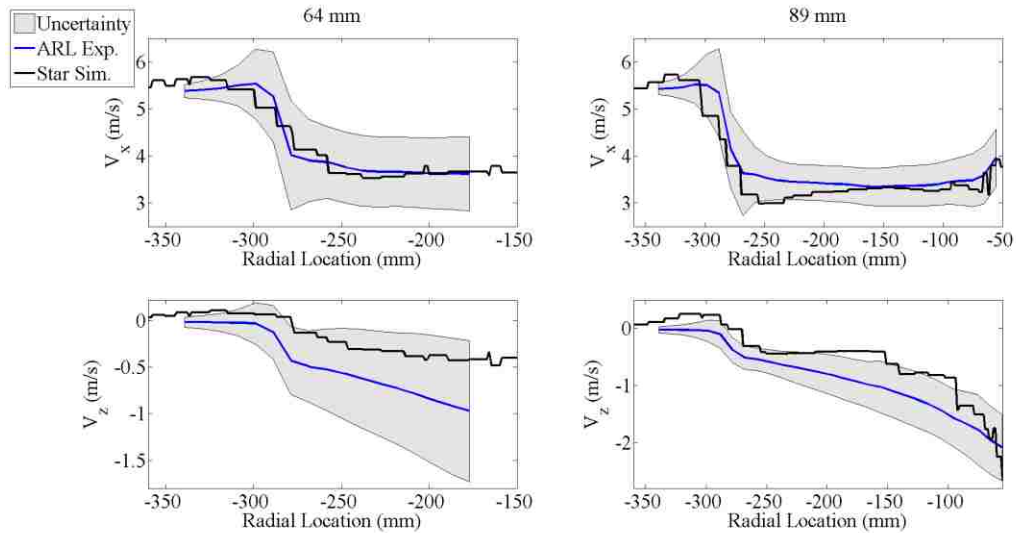


Figure 26: V_x and V_z velocity profiles with error in grey on experimental data for $x = 64$ mm and 89 mm

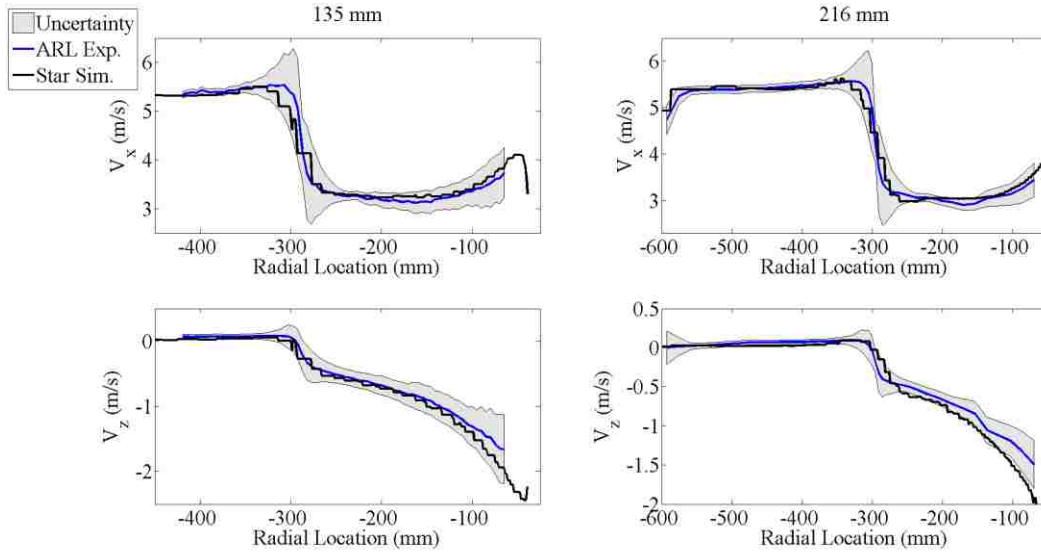


Figure 27: V_x and V_z velocity profiles with error in grey on experimental data for $x = 135$ mm and 216 mm

As stated earlier in the section *Velocity Profiles*, there is substantial uncertainty associated with the measurements taken at 250 mm. For instance, the radial velocity uncertainty at $y = 400$ mm had a measured velocity of nearly 0 m/s but could range from -1.7 to 1.7 m/s (Figure 28). Both this behavior and the large uncertainty associated with the experimental data are believed to be the result of near wall junction flow and measurement window assembly [8]. On the console side of the tunnel (i.e., negative transverse locations) the simulation results and experimental data have fair agreement at 574 mm (Figure 28). On the tower side (i.e., positive transverse locations) there is not good agreement between the simulation and experiment. This is most likely due to the simulation and mesh being unable to accurately resolve the flow structure in the downstream tower wake.

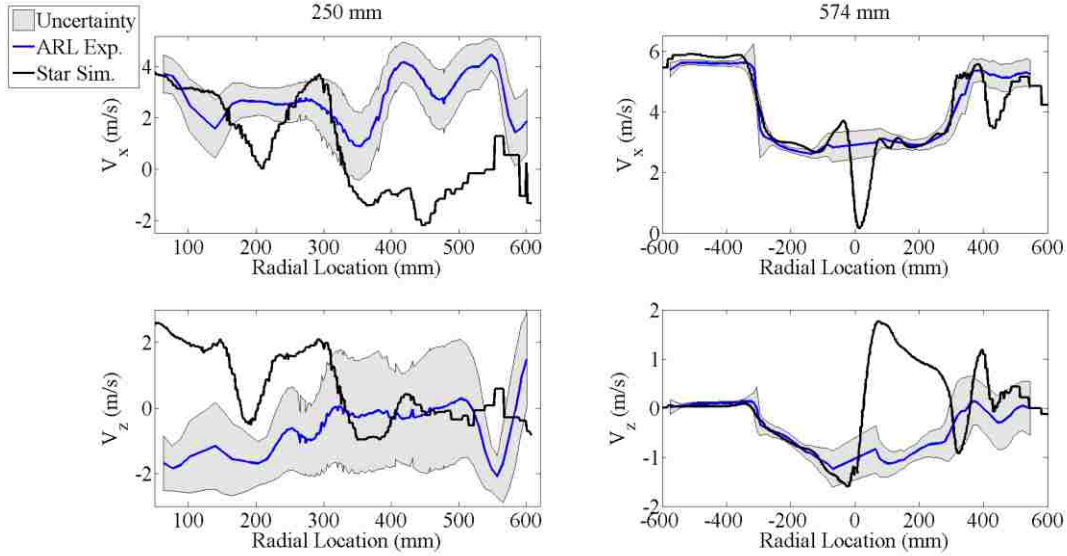


Figure 28: V_x and V_z velocity profiles with error in grey on experimental data for $x = 250$ mm and 574 mm

In Figure 29 the velocity profiles for $x=574$ mm and $z = \pm 19$ mm are shown for the simulation and experimental data with error bars. The simulation closely predicts the axial and radial velocity for $y=100-400$ mm. From $y=400-550$ mm the simulation results for radial velocity are within the experimental uncertainty bounds though this is not the case for the axial velocity.

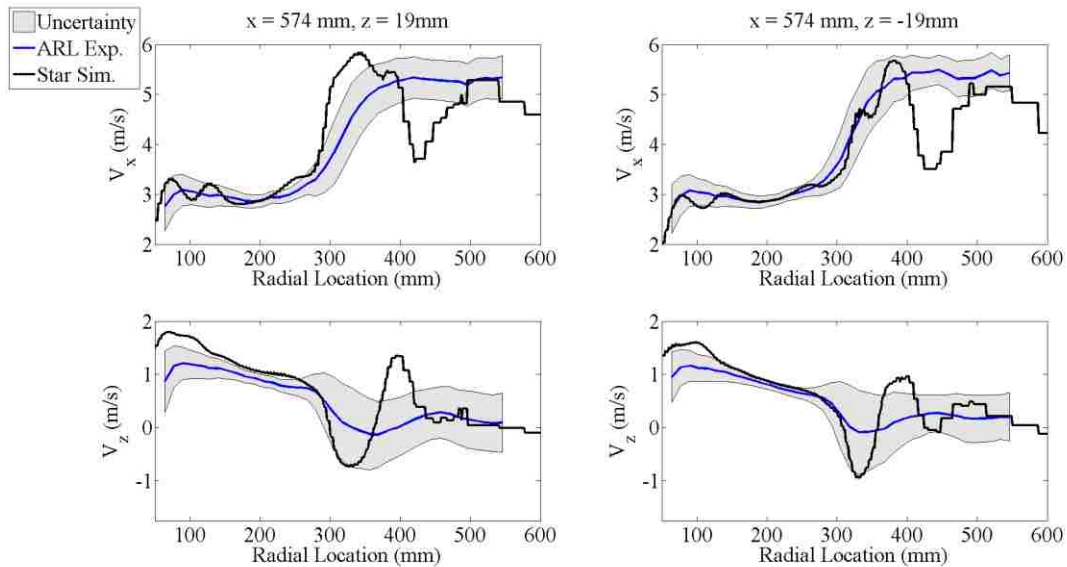


Figure 29: V_x and V_z velocity profiles with error in grey on experimental data for $x = 574$ mm and $z = 19$ mm and -19 mm

Quantifying the uncertainty in the experimental results indicates that the simulation results lie within the experimental error. Overall there is fair agreement between the simulation and experiment which supports the use of CFD simulations as complementary tool for flow analysis to experiments for current-driven MHK turbines.

V. Conclusion

Current-driven MHK devices are still in their infancy in regards to understanding the physics associated with them and developing an optimized design. Currently the primary method for quantifying the performance and flow characteristics of current-driven MHK devices is low-fidelity CFD models like WT_Perf [32] and CACTUS [33] with experimentation being used later however, the use of mid- and high-fidelity CFD could greatly reduce the time and expense associated with the combination of low-fidelity simulations and experiments. In this research an unsteady RANS simulation was run on an unstructured grid under experimental conditions of 5 m/s inflow, a turbine rotation rate of 664 RPM and a TSR of 4. The 2006 $k-\omega$ turbulence model was used because it is available in many commercial CFD packages and is well known for its ability to accurately predict the flow characteristics for a broad range of flow conditions.

The documented results illustrate that the CFD simulation and turbulence model were able to successfully capture the physical phenomena related to the flow past the Sandia turbine during the experiment. For all but a few circumstances, whose deviations were explained, the simulation was able to accurately calculate the performance coefficients, velocity profiles, Reynolds stress profiles and the unsteady tower pressures. The revolution averaged performance coefficients had very good agreement with experimental data with values differing by less than 0.27%. Single revolution performance coefficients agreed well with experimental data particularly for the drops in performance due to blade-tower interaction. The simulation was unable to predict the secondary drops in performance seen in the experiment however with improvements to the $k-\omega$ model or advanced models such as DES or LES the agreement may be improved.

Both axial and radial velocity profiles agreed well with experimental data except for the 250 mm survey location which is likely due to near wall junction flow and the window assembly of the experiment. Axial and radial Reynolds stress profiles of the simulation had fair agreement with experiments however, the simulation was unable to predict the peak Reynolds stress caused by shed vortices seen in the experiment. This shortcoming of the simulation may be remedied with changes to the 2006 $k-\omega$ models numerical scheme, specifically altering the stress-limiter term. The simulation captured the main behavior of the unsteady tower pressure seen in the experiment but with DES or LES modeling it is hopeful that the entire cyclic behavior can be captured. The uncertainty of experimental results was discussed which further illustrates sufficient agreement between the simulation and experimental results with most flow parameters lying within the experimental uncertainty.

This research illustrates the value of CFD as an inexpensive complementary analysis tool to use in conjunction with experimentation for evaluating and characterizing the behavior of axial-flow current-driven MHK turbines. High-fidelity CFD, as was performed in this research, is an attractive alternative to low-fidelity models but with an increase in cost. The benefits of high-fidelity CFD over low-fidelity models includes: better near- and far-wake characterization, flow recovery, blockage effects, and unsteady pressure characterization. It is important to note that regardless of the model, results from CFD cannot be used independent of experiments without a thorough verification and validation effort.

Future work may include evaluating additional turbulence models' ability to accurately predict the flow past an axial-flow water turbine as well as comparing

simulation data to other experimental data such as cavitation, turbine blade strain and acoustics. Additionally, it would be insightful to estimate the blockage effects of the experiment by removing the tunnel walls of the simulation and develop a system for blockage correction from this analysis. Flow recovery in the wake of the turbine would also be beneficial to study.

With this successful validation of the CFD simulation results it is hoped that the ARL experimental dataset can be provided to the research and industry communities for benchmarking new codes, design and optimization of new MHK devices, and for the establishment of industry and government standards.

VI. References

- [1] EPRI, "Assesment and Mapping of the Riverine Hydrokinetic Energy Resource in the Continental United States," EPRI, Palo Alto, CA, 2012.
- [2] EPRI, "Prioritized Research, Development, Deployment and Demonstration Needs: Marine and Other Hydrokinetic Renewable Energy," EPRI, Palo Alto, CA, 2008.
- [3] Sea Generation LTD., "Seageneration," Shiny Internet, 2007. [Online]. Available: <http://www.seageneration.co.uk/index.php>. [Accessed December 2014].
- [4] Openhydro, "Openhydro: a DCNS Company," [Online]. Available: <http://www.openhydro.com/home.html>. [Accessed December 2014].
- [5] Voith, "Voith: Ocean Energies," [Online]. Available: <http://voith.com/en/markets-industries/industries/hydro-power/ocean-energies-539.html>. [Accessed December 2014].
- [6] A. Bahaj, A. Molland, J. Chaplin and W. Batten, "Power and thrust measurements of marine current turbines under various hydrodynamic flow conditions in a cavitation tunnel and a towing tank," *Renewable Energy*, vol. 32, pp. 407-426, 2007.
- [7] S. Kang, I. Borazjani, J. A. Colby and F. Sotiropoulos, "Numerical simulation of 3D flow past a real-life marine hydrokinetic turbine," *Advances in Water Resources*, vol. 39, pp. 33-43, 2012.
- [8] A. A. Fontaine, W. A. Straka, R. S. Meyer and M. L. Jonson, "A 1:8.7 Scale Water Tunnel Verification & Validation Test of an Axial Flow Water Turbine," Pennsylvania State College, 2013.
- [9] E. Johnson, A. A. Fontaine, M. L. Jonson, R. S. Meyer, W. A. Straka, S. Young, C. van Dam, H. Shiu and M. Barone, "A 1:8.7 Scale Water Tunnel Test of an Axial Flow Water Turbine," in *1st Marine Energy Technology Symposium*, Washington, D.C., 2013.
- [10] T. P. Lloyd, S. R. Turnock and V. F. Humphrey, "Unsteady CFD of a Marine Current Turbine using OpenFOAM with Generalised Grid Interface," in *Proceedings of the 14th Numerical Towing Tank Symposium*, Poole, GB, 2012.
- [11] H. Shiu, C. van Dam, E. Johnson, M. Barone, R. Phillips, W. Straka, A. Fontaine and M. Jonson, "A Design of a Hydrofoil Family for Current-Drive Marine-Hydrokinetic Turbines," in *20th International Conference on Nuclear Engineering collocated with the ASME 2012 Power Conference*, Anaheim, 2012.

- [12] D. Mavriplis, "Unstructured Grid Techniques," *Annual Rev Fluid Mechanics*, vol. 29, pp. 473-514, 1997.
- [13] T. J. Baker, "Mesh generation: Art or Science?," *Progress in Aerospace Sciences*, vol. 41, pp. 29-63, 2005.
- [14] Star-CCM+, *Private correspondance with CD-Adapco regarding mesh statistics*, 2014.
- [15] D. C. Wilcox, *Turbulence Modeling for CFD*, DCW Industries, 2010.
- [16] S. Rodriguez, *ChNE 515-Computational Turbulence Modeling*, Albuquerque: University of New Mexico, 2014.
- [17] B. Launder and B. Sharma, "Appllication of the Energy Dissipation Model of Turbulence to the Calculation of Flow Near a Spinning Disc," *Letters in Heat and Mass Transfer*, vol. 1, no. 2, pp. 131-138, 1974.
- [18] T.-H. Shih, W. Liou, A. Shabbir, Z. Yang and J. Zhu, "A New k- ϵ Eddy Viscosity Model for High Reynolds Number Turbulent Flows -- Model Development and Validation," NASA-Technical Report, Cleveland, OH, 1994.
- [19] D. C. Wilcox, "Formulation of the k-w Turbulence Model Revisited," in *AIAA Journal-Aerospace Sciences Meeting and Exhibit*, California, 2007.
- [20] STAR-CCM+, "CD-Adapco: STAR CCM+," [Online]. Available: <http://www.cd-adapco.com/products/star-ccm%C2%AE>. [Accessed May 2014].
- [21] D. Wilcox, "Reassessment of the Scale-Determing Equation for Advanced Turbulence Models," *AIAA Journal*, vol. 26, no. 11, pp. 1299-1310, 1988.
- [22] B. Barney, R. Cunningham and K. Haskell, *Overview of the Computer Resource Team (CRT)*, Albuquerque: Sandia National Laboratories and Los Alamos National Laboratories, 2013.
- [23] Sandia National Laboraties and Pennsylvania State Advanced Research Laboratory, "Experimental Dataset," Pennsylvania State, Albuquerque, 2014.
- [24] P. Roache, "Quantification of Uncertainty in Computational Fluid Dynamics," *Annual Review of Fluid Dynamics*, vol. 29, pp. 123-160, 1997.
- [25] M. Lawson, Y. Li and D. Sale, "Development and Verification of a Computational Fluid Dynamics Model of a Horizontal-Axis Tidal Current Turbine," in *30th International Conference on Ocean, Offshore, and Arctic Engineering*, Rotterdam,

The Netherlands, 2011.

- [26] J. H. Matthews and K. D. Fink, Numerical Methods Using Matlab, Upper Saddle River, NJ: Prentice-Hall Pub. Inc., 2004, p. 355.
- [27] Matlab 2012b, *The Mathworks, Inc.*, Natick, Massachusetts.
- [28] S. B. Pope, Turbulent Flows, New York: Cambridge City Press, 2000.
- [29] P. Bernard, Turbulent Flow: Analysis, Measurement, and Prediction, Hoboken, NJ: John Wiley & Sons, Inc., 2002.
- [30] J. Dacles-Mariani, D. Kwak and G. Zilliac, "On numerical errors and turbulence modeling in tip vortex flow prediction," *International Journal for Numerical Methods in Fluids*, vol. 30, no. 1, pp. 65-82, 199.
- [31] J. R. Taylor, An Introduction to Error Analysis, Sausalito, CA: University Science Books, 1997.
- [32] M. L. Buhl, "WT_Perf User's Guide," National Renewable Energy Laboratory, 2012.
- [33] J. C. Murray and M. Barone, "CACTUS User's Manual," Sandia National Laboratories, Albuquerque, NM, 2013.
- [34] CD-Adapco, *User Guide: STAR-CCM+ Version 9.02*, CD-Adapco, 2014.